Density functional theory based study of methanation in the presence of subsurface atomic hydrogen on cobalt (0001) surface

A thesis submitted towards partial fulfilment of
BS-MS Dual Degree Programme

by

VIKAS NEGI

under the guidance of

AARTHI THYAGARAJAN

COMPUTATIONAL RESEARCHER, SHELL TECHNOLOGY CENTRE BANGALORE

Indian Institute of Science Education and Research Pune

May 5, 2014

Certificate

This is to certify that this thesis entitled "DENSITY FUNCTIONAL THEORY BASED STUDY OF METHANATION IN THE PRESENCE OF SUBSURFACE ATOMIC HYDROGEN ON Co(0001) SURFACE" submitted towards the partial fulfilment of the BS-MS dual degree programme at the Indian Institute of Science Education and Research Pune represents original research carried out by " Mr.VIKAS NEGI" at "SHELL TECHNOLOGY CENTRE BANGALORE", under the supervision of "Mrs. AARTHI THYAGARAJAN" during the academic year 2013-2014.

Student

VIKAS NEGI

Supervisor

AARTHI THYAGARAJAN

Certificate

This is to certify that this thesis entitled "DENSITY FUNCTIONAL THEORY BASED STUDY OF METHANATION IN THE PRESENCE OF SUBSURFACE ATOMIC HYDROGEN ON Co(0001) SURFACE" submitted towards the partial fulfilment of the BS-MS dual degree programme at the Indian Institute of Science Education and Research Pune represents original research carried out by " Mr.VIKAS NEGI" at "SHELL TECHNOLOGY CENTRE BANGALORE", under the supervision of "Mrs. AARTHI THYAGARAJAN" during the academic year 2013-2014.

Student

VIKAS NEGI

Supervisor

AARTHI THYAGARAJAN

Acknowledgements

I would like to thank my line manager Aarthi Thyagarajan and Computational Chemistry team lead Dr. Rajappan Vetrivel for their constant support and encouragement all throughout the project. I am also grateful to Dr. Leonardo Spanu and Dr. A.P.J Jansen both Computational researchers at Shell Technology Centre Bangalore for their valuable inputs. A big thanks to Dr Prasenjit Ghosh, IISER Pune for his supervision and help with a lot of ideas involved in the work. I also sincerely appreciate the help I got from Maselink Fokko, HPC systems engineer at Shell-Netherlands in configuring Quantum Espresso to efficiently run in parallel on the High Performance Computing cluster. Also, I would like to express my gratitude to the entire Computational Centre Of Expertise (CCOE) at Shell Technology Centre Bangalore for giving me the opportunity to work in such an intellectual environment and allowing me to access all the computational resources without any restriction. I am also indebted to IISER Pune for letting me join Shell Technology Centre Bangalore for my masters thesis. In the end, I would like to thank my family and friends for their love and support.

Abstract

It has been shown experimentally[1,2] that structural changes occur on the Cobalt catalyst surface under Fischer Tropsch (FT) conditions which lead to significantly enhanced reactivity. The reaction occurs at the length scale of an angstrom and time scale of 10^{-15} sec. To quantify this change in reactivity, properties such as bond lengths and energy of the molecules (in reactants, catalyst and products) need to be estimated. We have used *Density Functional Theory* as implemented in Quantum Espresso(QE)[3] to calculate the optimized adsorption geometries, adsorption energies and to determine the activation barriers for various pathways leading to methanation.

Earlier theoretical works have shown that subsurface hydrogen is an important species for methanation at FT conditions in Heavy Paraffin Synthesis (HPS) section of the Shell-GTL process.[4] Using DFT, it was reported that subsurface hydrogen enables a facile pathway from a chemisorbed surface methyl group to physisorbed methane. However, none of these studies were done at the *actual* CO coverages that might be present during FT conditions. Also, activation barriers for different pathways of methanation on a Co(0001) surface were *not* determined theoretically before. Similar studies[5] on Ni(111) indicate that the reaction might involve two transition states corresponding to a *resurfacing* barrier for the subsurface hydrogen and a *recombination* barrier for the methyl group and surface hydrogen. Hence, we have focused on this particular aspect of the methanation process on a Co(0001) surface.

We began with an extensive testing of different pseudopotentials. This was followed with a method and model verification for a Cobalt vacuum slab that was used to represent the catalyst surface. Later, we continued with an estimation of the adsorption energies of subsurface hydrogen at different coverages of $\theta = 0.11, 0.22, 0.33$ and 0.44 in the absence as well as the presence of surface CO at the realistic coverage of $\theta = 1/3$ and having the $(\sqrt{3} \times \sqrt{3})R30^o$ overlayer structure.

The next phase of the project involved doing a transition state search using the Climbing image-Nudged Elastic Band (CI-NEB)[15] method to determine the barriers for hydrogen dissociation and subsurface diffusion. The CI-NEB was again used to determine the *resurfacing* and the *recombination* activation barriers for methanation. *Density Functional Perturbation Theory (DFPT)* as implemented in the Phonon package within QE[3] was used to determine the normal modes of the initial, final as well as the transition state structures which was further used to make zero-point energy corrections to the activation barriers and also determine prefactors for the reaction rates as approximated within the *Harmonic Transition State Theory (hTST).*[7]

From our calculations, it can be inferred that presence of CO ($\theta = 1/3$) destabilizes the surface hydrogen. However, it does not have any appreciable effect on the stability of hydrogen present in the first, second and third sublayers. Hence, under the Fischer-Tropsch conditions subsurface hydrogen would still be stable as shown by earlier theoretical works.[4] Amongst the three different pathways considered for methanation, pathway-1 where a methyl group is adsorbed at a surface hcp site near a subsurface hydrogen resurfacing site had the overall lowest barrier. Continuing further, the *prefactors* and the *rate constants* for these pathways were estimated using the harmonic transition state theory (hTST) approximation[7] at a temperature of 500 K. After making the adequate zero point energy corrections to the activation barriers, the estimated rate constants again confirmed that pathway-1 was statistically the *most dominant* for methanation on a Co(0001) surface close to FT reaction temperatures.

Contents

Chapter 1

Introduction

1.1 Fischer-Tropsch (FT) technology

Almost all the major oil companies today use the Fischer-Tropsch (FT) reaction as the primary method for natural gas conversion to liquid petroleum.[2] In the first phase, natural gas is oxidised to yield a mixture of carbon monoxide and hydrogen which is also known as synthesis gas. FT synthesis usually forms the second phase, in which synthesis gas is converted into a mixture of primarily long straight chain paraffins with water as the main by-product. This is followed by the final step where these hydrocarbons undergo further hydrocracking to generate clean distillates as products. The entire process is pictorially depicted in fig 1.1

The conversion of syn gas to liquid hydrocarbons is a chain growth reaction of CO and H on the surface of a catalyst .

$$(2n+1)H_2 + nCO \rightarrow H-(CH_2)_n-H + nH_2O \tag{1.1}$$

These heterogeneous catalysts for industrial scale applications often consist of a *porous inorganic material* which is used[2] to support small metal particles. Using such an arrangement, a large surface area is available for catalysis. For reactions with a low *turnover number(the number of reactant molecules converted per surface metal site per second)*, a high density metal particle dispersion is needed. Also, different kinds of *promoters* can be added to enhance the catalytic activity. The structural inhomogeneity of such supported systems makes the problem of identifying the parameters to fine tune the catalytic performance increasingly complex! Such a knowledge would be quintessential for the development and optimization of catalysts on an industrial scale.

One way to reduce the level of complexity is to study *single crystal* metal surfaces.[2] The preparation of clean metal surfaces under ulta high vacuum (UHV) conditions has become very easy considering the technology available these days.[1] A lot of the work done has focused on studying the adsorption of molecules on these surfaces *starting from the gas phase.* These UHV systems are often combined with high pressure reaction cells so that the model catalysts can be studied at high temperature and pressure conditions which are usually present during catalysis. Cobalt has been one of the primary catalysts used for FT synthesis. It has a *high selectivity* for *chain growth reactions* and a low selectivity for the competing *water-gas shift reaction.* We have primarily focused our attention on the Co(0001) surface. It has been studied extensively[1] with in-situ PM-RAIRS, LEED and ex-situ STM and almost all the data is available in the open literature.

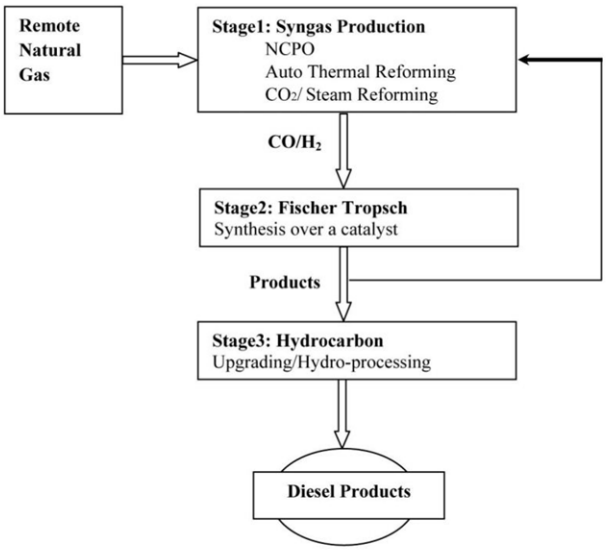

Figure 1.1: Conversion of natural gas into clean Diesel products

1.2 Methanation during Fischer-Tropsch (FT) synthesis

Low methane selectivity is one of the key requirements for a catalyst to have high efficiency during the FT synthesis. As we can see in the flow chart above, the starting material for gas-to-liquid (GTL) technology is natural gas which is mostly methane. An efficient syn gas production process would ensure that almost all the natural gas feed is converted to syn gas! Formation of methane [n=1 in the chain growth reaction (1)] again after FT synthesis is a *major problem* and makes the overall process ineffective.

1.2.1 Role of subsurface hydrogen in Ni(111)

A fundametal understanding of the exact methane formation mechanism is needed to improve the current efficiency of Cobalt catalysts. In this regard, the role played by subsurface hydrogen is significant primarily because of it's puzzling behaviour with Ni(111) surface. In a series of experiments , Ceyer and co-workers[8] have demonstrated that on Ni(111), subsurface hydrogen could hydrogenate adsorbed methyl to produce methane while surface hydrogen could not! Following on this work, it has been shown that subsurface hydrogen can hydrogenate other hydrocarbons as well while the surface hydrogen primarily remains inactive. Having pioneered the technique of synthesizing bulk deuterium in Ni under UHV conditions, Ceyer[8] observed that after adsorbing CH_3 and H species on the surface of the crystal and gradually heating it, the quadrupole mass spectrometer could only record the presence of CH_3D species at a thermal desorption temperature of 180 K. An auger spectrum measured after ramping the crystal to 200K, just beyond the desorption temperature of CH_3D showed that all of the 0.15 ML of carbon had been removed by the formation of CH_3D species.[8] Similar experiments have been carried out in the absence of bulk deuterium or hydrogen but in the presence of surface bound deuterium or hydrogen. Adsorbed methyl radicals are produced by the dissociative chemisorption of CH_4 on a clean surface. The surface was then exposed to

molecular deuterium or hydrogen which resulted in the formation of 0.85 ML of adsorbed H or D. Ramping the crystal temperature at a rate of 2 Ks^{-1} , the thermal desorption spectra was recorded and no evidence for methane formation was seen. These results conclusively demonstrate the importance of bulk species as reactants in heterogeneous catalysis. Various theoretical studies have been done to explain the physical origin of the high reactivity of subsurface H in Ni.[5] Density Functional Theory (DFT) based calculations coupled with various transition state search algorithms have been successfully applied to identify the low-energy pathways for the hydrogenation of methyl on Ni(111) surface. It has been shown that subsurface hydrogen at different sites have very *different* activation barriers towards methanation, depending on their relative position to the adsorbed methyl group.[5]

Since, Ni and Co occur besides one another in the periodic table and are known to have similar catalytic properties, it would be very interesting to see whether bulk hydrogen can play a similar role during methane formation in FT synthesis using Co catalysts.

1.2.2 Our motivation

Subsurface hydrogen has been shown to exist theoretically for Cobalt catalysts under the Fischer-Tropsch conditions.[4] In-house experiments that have followed this work have shown indications that the predictions might be fairly accurate. However, there is still a lack of understanding about the stability of subsurface hydrogen in the presence of CO. Also, there are no known literature references related to the characterization of methanation pathways on Co(0001) surface involving subsurface hydrogen. DFT has long been established as a reliable method to estimate adsorption energies and in conjunction with other optimization methods to determine normal modes and saddle points on the potential energy surface. We wanted to conduct extensive DFT-based calculations to study the stability of subsurface hydrogen in the *presence* of realistic CO coverage. This was to be followed by the determination of methanation pathways involving subsurface hydrogen using the Nudged Elastic Band method. In our project, we have specifically focused on the final step of the methanation process i.e reaction between CH_3 and H, since it has been shown conclusively[9] that the barrier for this final step is the highest amongst all the hydrogenation steps with carbon and hence is the *rate limiting* step.We had also planned to conduct extensive Density Functional Perturbation Theory (DFPT) based calculations to do a normal mode analysis of the initial and the transition state structures which would further help us determine the prefactors and estimate the rate constants for (methyl+H) combination events within the Harmonic Transiiton State Theory (hTST) approximation close to the FT temperatures.

Chapter 2

Theory

2.1 Density Functional Theory

The Density Functional Theory (DFT) is one of the most successful methods used to compute the properties related to the electronic structure of matter. It has a wide range of applicability that includes atoms, molecules, quantum and classical fluids etc. DFT is used to predict properties such as molecular structures, ionization and electron gain enthalpies, vibrational frequencies, electric and magnetic properties and activation barriers for catalytic reactions. The original DFT has been generalized to deal with many different systems such as spin polarized systems, free energy calculations at finite temperatures, superconductors with electron pairing, relativistic electrons, time dependent phenomenon and excited states. Within DFT itself, there are a number of approximations that are used depending on the type of system studied and the amount of accuracy needed. There is almost always a trade off between computational time and the accuracy required! More efficient algorithms are being implemented that take less time and give more accurate results. DFT is similar to the Hartree-Fock method in many respects. However, there are some fundamental differences between the two.

2.2 Formulation of DFT

The Hartree-Fock methods usually involved the explicit calculation of the quantum mechanical wavefunction ψ which itself has very little meaning. We are usually interested in the probability density$|\psi|^2$. Solving the Schrodinger equation is computationally very demanding. There was a need for a way where we could calculate an observable without using the Schrodinger equation. The quantity of interest in DFT is the electron density $\rho(r)$ where r is the position vector. It is defined as the integral over the spin coordinates of all electrons and over all but one of the spatial variables $\rho(r) = N \int .... \int |\psi(x_1, x_2....x_N)|^2 ds_1 dx_2 ... dx_N$. In other words, $\rho(r)$ determines the probability of finding any of the N electrons within volume element dr. The electron density $\rho(r)$ is defined in such a way that it satisfies the following properties: $\rho(r \to \infty) = 0$ and $\int \rho(r) dr = N$, where N is the total number of electrons. The electron density is an observable which has more physical meaning than the wavefunction ψ.The total energy of the system can then be written entirely in terms of the electron density $\rho(r)$ and hence solving for $\rho(r)$ would give us all the information that we need about the system.

2.2.1 The first Hohenberg-Kohn theorem

This theorem[10] demonstrates that the electron density can be used to uniquely determine the Hamiltonian of the system and hence all the other desired properties. Stated otherwise, the external potential $V_{ext}(r)$ is (within a constant) a unique functional of $\rho(r)$. However, this theorem talks only about the *ground state* of the system and cannot directly be applied to an excited state. The total energy can now be written as $E[\rho] = T[\rho] + E_{NE}[\rho] + E_{ee}[\rho]$,where $T[\rho]$ is the kinetic energy of the system, $E_{NE}[\rho]$is the electron-nucleus interaction and $E_{ee}[\rho]$is the electron-electron interaction energy. The nuclear kinetic energies are ignored due to the Born-Oppenheimer approximation. The total energy is further simplified as $E[\rho] = \int \rho(r)V_{NE}(r)dr + F_{HK}[\rho]$ where $F_{HK}[\rho] = T[\rho] + E_{ee}[\rho]$. The functional $F_{HK}[\rho]$ is completely universal and can be applied to any type of system at hand! The explicit form of this functional is the core area of research in DFT. The electron-electron interaction can be split into a classical and a non-classical part. $E_{ee}[\rho] = J[\rho] + E_{ncl}[\rho]$ where $J[\rho] = \frac{1}{2}\int\int \frac{\rho(r_1)\rho(r_2)}{r_{12}} dr_1 dr_2$ is the classical expression and E_{ncl} is the non-classical contribution that results from self-interaction, exchange and coulomb correction terms. The explicit form of the functionals $T[\rho]$ and $E_{ncl}[\rho]$ are unknown!

2.2.2 The second Hohenberg-Kohn theorem

If the input electron density is the true ground state density then and only then the functional $F_{HK}[\rho]$ would evaluate to the *lowest energy* of the system. Any other electron density would give an energy that is higher than the ground state energy.[10] This is essentially a variational principle for the electron density $\rho(r)$. $E[\rho^*] \geq E_o$where E_o is the true ground state energy of the system. For any trial electron density $\rho^*(r)$ which satisfies the required boundary conditions $\rho^*(r) \geq 0$ and $\int \rho^*(r)dr = N$, the energy obtained from the total energy functional $E[\rho^*]$ represents an upper bound to the true ground state energy E_o. Once again this variational principle is valid only for the ground state and cannot be used for evaluating excited states!

2.2.3 The Kohn-Sham equations

The ground state energy of the system can be written as $E_o = min_{\rho\to N}(F[\rho] + \int \rho(r)V_{NE}dr)$. The universal expression $F[\rho]$ contains the unknown $T[\rho]$and $E_{ncl}[\rho]$. To solve this issue Kohn and Sham proposed[10] to calculate the exact kinetic energy of a non-interacting reference system with the same density$\rho(r)$ as the real one. The kinetic energy of the reference system is calculated as $T_s = \frac{-1}{2}\sum < \psi_i|\nabla^2|\psi_i >$and the density as $\rho_S(r) = \sum\sum_s |\psi_i(r,s)|^2 = \rho(r)$. The $\psi_i$are the orbitals of the reference system. Here, T_S is not the kinetic energy of the real system. It is the exact kinetic energy of the reference non-interacting system. The following separation accounts for this fact where $F[\rho] = T_S[\rho] + J[\rho] + E_{XC}[\rho]$, the $E_{XC}[\rho]$ is the exchange-correlation energy and contains all the unknowns embedded within itself! Rearranging terms we get $E_{XC}[\rho] = (T[\rho] - T_S[\rho]) + (E_{ee}[\rho] - J[\rho])$.

The energy of the interacting system can be written as $E[\rho] = T_S[\rho] + J[\rho] + E_{XC}[\rho] + E_{Ne}[\rho]$ which can be further expanded in terms of the orbitals ψ_i. The term E_{XC} has no explicit form! Other than that, the energy functional can be put under the constraint $<\psi_i|\psi_j >= \delta_{ij}$and minimized thus resulting in a set of equations known as the Kohn-Sham

equations. They have the following form:

$$(\frac{-1}{2}\nabla^2 + V_s(r_1))\psi_i = \epsilon_i\psi_i \tag{2.1}$$

where $V_s(r_1) = \int \frac{\rho(r_2)}{r_{12}}dr_2 + V_{XC}(r_1) - \sum \frac{Z_A}{r_{1A}}$, $V_{XC} = \frac{\delta E_{XC}}{\delta\rho}$ these equations need to be solved iteratively. The approach is called a self-consistent field (scf) approach. The Kohn-Sham orbitals as such don't have much of a physical significance. However, an analogue of Koopman's theorem exists for this case too! The highest occupied orbital energy ϵ_{max}equals the ionization enthalpy of that system.

2.3 Approximations for E_{XC} within DFT

2.3.1 The Local Density Approximation (LDA)

The exchange-correlation energy E_{XC} is an unknown and various attempts have been made to approximate its functional form. One such way[10] is to use the model of an uniform electron gas. The exchange correlation energy can be written as $E_{XC}^{LDA}[\rho] = \int \rho(r)\epsilon_{XC}(\rho(r))dr$ where $\varepsilon_{XC}(\rho(r))$ is the exchange correlation energy per particle of an uniform electron gas of density $\rho(r)$. This density in a uniform gas would have the same value at every position. The quantity $\varepsilon_{XC}[\rho(r)]$ can be further expanded as $\varepsilon_{XC}[\rho(r)] = \varepsilon_X[\rho(r)] + \varepsilon_C[\rho(r)]$,the exchange part $\varepsilon_X$was computed by Bloch and Dirac and the value for a unifrom electron gas was shown to be $\epsilon_X = \frac{-3}{4}(\frac{3\rho(r)}{\pi})^{\frac{1}{3}}$. No such explicit expression has been derived for the $\varepsilon_C$which is mainly due to its complex nature arising out of quantum interactions. The accuracy of the LDA is not very good as the uniform gas approximation is hardly found in any practical system. Some literature suggests that LDA gives bond lengths of molecules and solids in certain systems with an amazing accuracy of ~ 2% .[1] However, LDA mostly fails in solid state systems dominated heavily by electron-electron interactions.

2.3.2 The Generalized Gradient Approach (GGA)

To account for the non-homogeneity of the electron distribution in real systems, it was suggested to formulate the electron correlation energy in terms of the gradient of the electron density.[10] The electron correlation energy has the form $E_{XC}^{GGA} = \int f(\rho_\alpha, \rho_\beta, \nabla\rho_\alpha, \nabla\rho_\beta)$. We can also form hybrid functionals such as $E_{XC}^{hybrid} = \alpha E_X^{KS} + (1-\alpha)E_{XC}^{GGA}$ where $E_X^{KS}$is the exchange calculated with the exact KS wave function and α is a fitting parameter. It essentially gives weight to the individual components in the hybrid functional. The accracy of the hybrid orbitals is better compared to LDA and the normal GGA functional. Another way to improve upon the GGA would be to take the second derivative of the electron density into consideration. Such functionals involving the Laplacian are termed as meta-GGA. However, numerically calculating the laplacian is not easy and hence the improved accuracy over GGA is clouded by this drawback!

2.4 The Pseudopotential Approximation

A solid can be considered as a collection of valence electrons and ion cores. The ion cores consist of the nuclei and tighly bound core electrons. In the pseudopotential approach

employed in the DFT package Quantum Espresso, the ion cores are considered to be *static*! This is based on the assumption that the ion cores are not involved in chemical bonding and remain more or less unchanged during a chemical reaction. In order to satisfy the orthogonality constraint, the all-electron wavefunctions of the valence-electrons exhibit rapid oscillations in the core region. When we try to represent such functions using plane waves, the size of the basis set becomes too large! The pseudopotential approach is used to solve this problem.[13] Here, the core electrons and the strong coulomb potential are replaced by a weaker pseudopotential that acts on a set of pseudofunctions. This potential can be represented using a *small* number of fourier components. Pseudopotentials ideally have *no nodes* within the core region and thus require a small basis set. Smaller basis sets reduce computational times and allow us to deal with bigger systems involving more complex calculations.

Pseudopotentials are usually constructed in a way such that the *scattering properties* of the full ionic potential are reproduced. The scattering from the pseudopotential is angular momentum dependent. A pseudopotential is considered *soft* when it requires a small number of fourier components for it's accurate representation and *hard* otherwise. The early norm-conserving pseudopotential developed for the transition metals were extremely hard and hence computationally time consuming. As suggested by Vanderbilt (1990), the norm conserving constaint can be relaxed to generate much softer pseudopotentials. In the ultrasoft pseudopotential scheme, the pseudo-wavefunctions are allowed to be as soft as possible within the core region, so the the energy cut-offs are reduced dramatically. Ultrasoft pseudopotential have another advantage.[13] The generation algorithm ensures *good* scattering properties over a well defined energy range which results in much better accuracy and transferability of the pseudopotential. Ultrasoft pseudopotential also treats shallow core states as valences by including multiple sets of occupied states in each angular momentum component. This adds to it's high accuracy. *Transferability* is the main requirement of all pseudopotential techniques over all types of DFT implementations. Pseudopotentials are usually constructed from a fixed configuration of an isolated atom or ion and thus they are expected to reproduce the scattering properties of a nucleus in that particular configuration. The pseudopotential should also give reliable results for other atomic configurations. Good pseudopotentials can be applied across a diverse range of systems such as molecules, slabs, bulk etc.

2.4.1 Classification of Pseudopotentials

The degree of hardness of a pseudopotential quantifies the number of fourier components needed for it's accurate representation. A pseudopotential is considered *soft* when it requires a small number of fourier components. As this number increases, it becomes progressively *harder!* Pseudopotentials are broadly classified as Norm-preserving and Ultrasoft.

2.4.1.1 Norm-preserving Pseudopotential

They are constructed[13] by enforcing the condition that outside the cutoff radius, the norm of the pseudopotential approaches that of the corresponding one electron wavefunction. It has been shown by that for Pseudo and all electron wavefunctions to be identical beyond the cutoff radius , it is necessary for the integrals of the squared amplitudes of the two functions to be the same $\int_0^{r_c} r^2|\psi_{nl}^{ps}(r)|^2dr = \int_0^{r_c} r^2|\psi_{nl}^{ae}(r)|^2dr$ which also implies

charge contained in the region for $r < r_c$ is the same.[13] Pseudopotentials with large cutoff $r_c$are usually softer i.e. rapidly convergent but have less transferable characteristic. *Transferability* is the ability of the pseudopotential to produce accurate and realistic results in different environments. Hence, there is a trade off between the transferability needed and the degree of hardness present in the pseudopotential.

2.4.1.2 Ultrasoft pseudopotential

This form of the potential was first suggested by Vanderbilt(1990) and involves relaxing the norm conserving requirement in order to generate really soft pseudopotentials. A high cutoff energy is required for the plane wave basis set when there are tighly bound orbitals that have a large fraction of their weight inside the core region of the atom. The only way to reduce the size of the basis set would be to remove the charge associated with these tightly bound orbitals from the core region. Hence,the pseudopotentials are allowed to be as soft as possible in the core region so that the cutoff energy gets drastically reduced! The electron density can be divided into two parts: the soft part extending through the unit cell and the hard part localized at the ionic core. These potentials are known to converge very rapidly and hence have found widespread use in DFT calculations. Their accuracy is usually better than Norm-preserving pseudopotentials!

2.4.2 Construction of Pseudopotentials

2.4.2.1 Constructing a Norm-preserving pseudopotential

First, all electron calculations are carried out for an isolated atom in a particular configuration which may not necessarily be the ground state. This provides valence electron eigen values and wave functions for the atom. Then a parametrised form for the ionic pseudopotential is chosen. The parameters are then adjusted[13] and optimized such that a pseudoatom calculation with the same exchange correlation potential as the all electron atom gives pseudo-wavefunctions ψ_{ps} that match to the valence wavefunctions outside a cutoff radius $r_c$and pseudo-eigenvalues that are equal to the valence eigenvalues. The procedure involves direct inversion of the Kohn-sham equations in the radial coordinates. The ionic pseudopotentials are constructed with the cutoff radius $r_c$set to 2-3 times the physical core radius. The smaller the value of r_c,the *harder* and more *transferable* the pseudopotential is!

2.4.2.2 Constructing an Ultrasoft pseudopotential

An all-electron calculation is carried out on the free atom which leads to a screened atomic potential $V_{AE}(r)$.For each angular momentum, a set of reference energies, ϵ_l, is chosen. These energies are chosen in such a way that all the scattering properties are adequately covered. At each reference energy, solution to the radial Kohn-Sham equations is obtained which is also regular at the origin. A cutoff radius $r_{cl}$is chosen and for every all-electron wavefunction ψ, a pseudo-wavefunction $\phi$is constructed subject to the constraint that it smoothly joins ψ at the cutoff radius r_{cl}. A smooth local potential $V_{loc}(r)$ is generated to match the all-electron potential $V_{AE}(r)$ at a cutoff radius r_{loc}. In this procedure it is ensured that the scattering properties are correct at each reference energy. The transferability can thus be improved by increasing the number of such energies. Also,

the pseudovalence charge density is precisely equal to the all-electron valence density in the reference isolated atom.

2.5 Brillouin zone sampling

The infinite system is modeled using an array of primitive cells $N_{cells} = N_1N_2N_3$ where N_i are the number of cells along the primitive vector directions $a_i(i = 1, 2, 3)$. Using the generalized Born-Von Karman boundary conditions:

$$\psi(r + N_i a_i) = \psi(r)$$

where $i = 1, 2, 3$. Applying Bloch theorem[13] (see appendix A) to the above equation, we get $\psi(r+N_i a_i) = exp(iN_i k\cdot a_i)\psi(r)$ which restricts the valus of k such that $exp(iN_i k\cdot a_i) = 1$. Therefore, the values of $\{x_i\}$ are real and equal to $x_i = \frac{l_i}{N_i}$ where $i = 1, 2, 3.$ and the $\{l_i\}$ are integers. The bloch wave vectors can now be written as $k = \sum_1^3 \frac{l_i}{N_i} g_i$. Even if we set the limit for an infinite crystal $N_i \to \infty$,the number of k-points form a *countably infinite* set. Also, the k vectors that differ only by a reciprocal space vector G are equivalent. Hence, we can focus only on the wavevectors that lie within the *first Brillouin zone.* Any vector that lies outside this zone can be translated using an operator and moved within the zone. In order to construct the density, we must evaluate the eigenstates at the k-vectors within this zone. Since the wavefunctions and the Hamiltonian eigenstates vary smoothly within the Brillouin zone, only a finite number of points need to be chosen for obtaining maximum efficiency! From the values of the wavefunctions at a certain set of k=points, the values at nearby k-points can also be approximated using perturbation theory. The volume of a Brillouin zone is related to the cell size as $\Omega_{BZ} = \frac{(2\pi)^3}{\Omega_{cell}}$. As we can see, for very large systems the Brillouin zone volume is very small. Hence, only a few k-points need to be considered for evaluating the observables.

2.5.1 The Monkhorst-Pack scheme

It is a particular scheme[14] devised to do Brillouin zone integration efficiently. The k-points are chosen as $k = \sum_{i=1}^3 \frac{2n_i - N_i - 1}{2N_i} b_i$, $n_i = 1, 2....N_i$. Symmetry arguments are often used to reduce the number of k-points needed for evaluating the observables. The electron density functional is evaluated by integrating over the first Brillouin zone $n(r) = \frac{1}{\Omega_{FBZ}} \sum_i^{occ} \int_{FBZ} n_{ik}(r)dk$ where $n_{ik}(r) = |\psi_{ik}(r)|^2$. This can be shown to be equivalent to $n(r) = \frac{1}{N_k} \sum_k \sum_i^{occ} n_{ik}(r)$. A mesh with uniformly spaced k-points is usually preferred! Once, the points are classified according to their respective symmetries, the electron density functional can be evaluated as $n(r) = \sum_k \omega_k \sum_i^{occ} n_{ik}(r)$ where the

$$\omega_k = \frac{Number - of - symmetry - connected - k - points}{Total - number - of - k - points - in - FBZ} \tag{2.2}$$

The greater the k-point density, the more precise are the results! Thus, by confining the calculations only to the *First Brillouin zone (FBZ),* a lot of computational time is saved!

2.6 Smearing method for metals

The fermi level ε_F is defined as the energy of the highest occupied state at zero kelvin temperature. The position of fermi level differs based on whether the material under

consideration is a metal, insulator or a semiconductor. For insulators and semiconductors, there is a finite gap between the valence and the conduction bands. The electron density of states goes smoothly to zero at the gaps! Since electrons are fermions, the occupation number is either 0 or 1. At 0 K, the distribution function is a step function going abruptly from 1 to 0 at the fermi energy. Since the evaluation of the measurable properties involves integration over all the wavevectors, we need to include a lot of k-points to account for the discontinuity in k-space between the occupied and the unoccupied states[13]. This can also lead to convergence problems while running a self consistent field loop! The solution to this problem is called 'smearing'. In the smearing method, the step function is *replaced* with a smoother function which would allow for partial occupation of states around ε_F. The smearing methods are of various kinds and their usage depends on the type of system involved.

2.6.1 Gaussian smearing

The smearing function is defined as $f_{ik}\left(\frac{\varepsilon-\mu}{\sigma}\right) = \frac{1}{2}[1 - erf(\frac{\varepsilon-\mu}{\sigma})]$ where erf is an error function. The total energy is no longer variationally minimal in this case. It has to be replaced by a free energy $F = E - \sum_{nk} w_k \sigma S(f_{nk})$. The forces would now be the derivatives of this free energy! The physical significance of such a free energy is not very clear in the case of Gaussian smearing. It is more like a mathematical simplification done to obtain faster convergence! However, the value for $\sigma = 0$ can be found from a finite T calculation using extrapolation methods $E(\sigma \to 0) = E_0 = \frac{1}{2}(F + E)$. This could serve as a reasonable method to associate physical significance to a finite temperature free energy calculation.

2.7 Density Functional Perturbation Theory (DFPT)

All phonon calculations start from the self consistent charge density and Kohn-Sham orbitals calculated for the equilibrium positions of the atomic species involved. The phonon calculations make use of DFPT which is just an extension to the well established framework of DFT.[13] As we already know, many physical properties depend upon a system response to some form of perturbation. Examples include phonons, polarisibilities, Raman intensities, IR cross sections etc. Within DFPT, the system response is calculated through a series of single point calculations carried out at varying strengths of the external perturbation. The method appears to be crude and complex. They are sometimes restricted in applications; for example they might require really large computational resources to calculate the response properties at some arbitrary wave vector q. However, the phonon calculation algorithms have been improved a lot and lately DFPT has proven to be of immense importance in understanding the quantum mechanical mechanisms behind such processes as well as a rigorous testing ground for theoretical models.

2.7.1 Theory behind DFPT

Within the framework of DFT, the energy of a system is written as a functional of the electron density $n(r) : E = T_s[n(r)] + E_H[n(r)] + E_{xc}[n(r)] + \int n(r)V(r)dr$. This energy is minimized by the ground state charge density. The Kohn-Sham (KS) equation for one electron orbital are : $(H_{KS} - \epsilon_i)\psi_i(r) = 0$; $H_{KS} = \frac{-\hbar^2}{2m}\nabla^2 + V_H(r) + V_{xc}(r) + V(r)$. These are solved self consistently and the charge density is given by $n(r) = \sum_v |\psi_v(r)|^2$ where

the sum is over the occupied states. The Hartree and exchange-correlation potentials are defined as:

$$V_H(r) = \frac{\partial E_H[n(r)]}{\partial n(r)} = e^2 \int \frac{n(r^{'})}{|r - r^{'}|} dr^{'},$$

$$V_{xc}(r) = \frac{\partial E_{xc}[n(r)]}{\partial n(r)}$$

Let us assume that the external potential depends on some parameter λ.

$$V_\lambda(r) \simeq V(r) + \lambda \frac{\partial V(r)}{\partial \lambda} + \frac{1}{2}\lambda^2 \frac{\partial^2 V(r)}{\partial \lambda^2} + ...$$

The derivatives are calculated at $\lambda = 0$ and the charge density is expanded as:

$$n_\lambda(r) \simeq n(r) + \lambda \frac{\partial n(r)}{\partial \lambda} + \frac{1}{2}\lambda^2 \frac{\partial^2 n(r)}{\partial \lambda^2} + ...$$

The energy functional is also expanded into the powers of λ.

$$E_\lambda \simeq E + \lambda \frac{\partial E}{\partial \lambda} + \frac{1}{2}\lambda^2 \frac{\partial^2 E}{\partial \lambda^2} + ...$$

The first order derivative $\partial E/\partial\lambda$ does not depend on any derivative of $n(r)$. From the Hellmann-Feynman theorem it can be shown that: $\frac{\partial E}{\partial \lambda} = \int n(r) \frac{\partial V(r)}{\partial \lambda} dr$.

The second order derivative $\partial^2 E/\partial\lambda^2$ depends on the first order derivative of the charge density, $\partial n(r)/\partial\lambda$:

$$\frac{\partial^2 E}{\partial \lambda^2} = \int \frac{\partial V(r)}{\partial \lambda} \frac{\partial n(r)}{\partial \lambda} dr + \int n(r) \frac{\partial^2 V(r)}{\partial \lambda^2} dr$$

The result can be generalized to mixed derivatives:

$$\frac{\partial^2 E}{\partial \lambda \partial \mu} = \int \frac{\partial V(r)}{\partial \lambda} \frac{\partial n(r)}{\partial \mu} dr + \int n(r) \frac{\partial^2 V(r)}{\partial \lambda \partial \mu} dr$$

The quantity of interest now is the first order derivative of the charge density. It can be obtained using linear response theory and applying perturbation theory to the Kohm-Sham hamiltonian.

$$\frac{\partial \psi_v(r)}{\partial \lambda} = \sum_c \psi_c(r) \frac{1}{\epsilon_v - \epsilon_c} < \psi_c | \frac{\partial V_{KS}}{\partial \lambda} | \psi_v > = \frac{1}{\epsilon_v - H_{KS}} P_c \frac{\partial V_{KS}(r)}{\partial \lambda} \psi_v(r)$$

Here, v denotes the occupied KS states and c denotes the empty ones! P_c is the projector over empty states. The self consistent potential response $\partial V_{KS}/\partial\lambda$ can be expanded as:

$$\frac{\partial V_{KS}(r)}{\partial \lambda} = \frac{\partial V(r)}{\partial \lambda} + \int \frac{1}{|r - r'|} \frac{\partial n(r^{'})}{\partial \lambda} dr^{'} + \int \frac{\delta V_{xc}(r)}{\delta n(r^{'})} \frac{\partial n(r^{'})}{\partial \lambda} dr^{'}$$

which depends on the first order variation $\partial n(r)/\partial\lambda$of the charge density :

$$\frac{\partial n(r)}{\partial \lambda} = 2Re \sum_v \psi_v^*(r) \frac{\partial \psi_v(r)}{\partial \lambda}$$

The quantity $\partial\psi_v(r)/\partial\lambda$and other needed ones can thus be determined by the solution of a self-consistent set of linear equations.

2.7.2 Normal vibrational modes in crystals and molecules

Phonons are the collective vibrations that occur in a periodic arrangement of atoms or molecules in condensed matter, such as solids and some liquids. It represents an excited state in the quantization of the vibrational modes in the solid. It is often considered to be a quasiparticle. The relation between the frequency $\omega$and the wavevector k of a phonon is known as the dispersion relation. Depending on the relative motion of atoms in a periodic system we have acoustic and optical modes. As the name suggests acoustic modes are related to sound. They are responsible for the propagation of sound in a solid and hence have long wavelengths and low frequency! The optical modes are activated when the solid interacts with high frequency electromagnetic radiation. Experimentally, phonon dispersion curves are measured using neutron scattering.

The normal mode frequencies ω, displacement patterns U_I^α for the cartesian component $\alpha$of an atom I, at atomic position R_I, are determined by the secular equation:

$$\sum_{J,\beta}(C_{IJ}^{\alpha\beta} - M_I\omega^2\delta_{IJ}\delta_{\alpha\beta})U_J^\beta = 0$$

where $C_{IJ}^{\alpha\beta}$ is a matrix of inter-atomic force constants (IFC) which are the second derivatives of energy with respect to atomic positions: $C_{IJ}^{\alpha\beta} = \frac{\partial^2 E(R)}{\partial R_I^\alpha R_J^\beta}$. In crystals, normal modes are classified based on the wavevector q. Phonon frequencies $\omega(q)$ and displacements $U_s^\alpha(q)$ are determined by the secular equation:

$$\sum_{t,\beta}(\acute{C}_{st}^{\alpha\beta}(q) - M_s\omega^2(q)\delta_{st}\delta_{\alpha\beta})U_t^\beta(q) = 0$$

We now introduce monochromatic perturbation u to the atomic positions $R_I = R_l + \tau_s$ as $R_I[u_s(q)] = R_l + \tau_s + u_s(q)e^{iq\cdot R_l}$ where $R_l = lattice$ vector, $\tau_s =$ equilibrium position of the s-th atom in the unit cell. This introduces a response having the same wavevector q at linear order. The Fourier transforms of the force constants at q are the second derivatives of energy with respect to such monochromatic perturbations:

$$\dot{C}_{st}^{\alpha\beta}(q) = \sum_R e^{-iq\cdot R}C_{st}^{\alpha\beta}(R) = \frac{1}{N}\frac{\partial^2 E}{\partial u_s^{\star\alpha}(q)\partial u_t^\beta(q)} \tag{2.3}$$

The second derivative of the energy can be calculated using DFPT as shown in the previous section. All we need is the linear response $\partial n(r)/\partial u_s^\alpha(q)$. Adequate diagonalization will give us the phonon modes at a wavevector q. The calculation of the inter-atomic(real space) force constants is done using the following two steps:

- calculate $\acute{C}_{st}^{\alpha\beta}(q)$on a suitable grid of q vectors.
- Fourier transform to the real space.

The denser the grid of q vectors the larger the vector R for which the inter atomic force constants are calculated. For non polar systems, inter atomic force constants are relatively short ranged , thus requiring only a small number of calculations at different q. Once the inter-atomic force constants are known, phonon modes can be calculated at any q vector. Repeating such single point calculations at different q values gives the entire phonon dispersion curve!

The intensity of the IR modes are calculated as:

$$I_{IR}(\nu) = \sum_{\alpha} |\sum_{s\beta} Z_s^{\star\alpha\beta} U_s^{\beta}(\nu)|^2 \tag{2.4}$$

which also makes use of the effective charges and phonon displacement patterns. All this information is stored in the dynamical matrix that is generated after a vibrational calculation is done using ph.x executible. The non-resonant raman intensities are also estimated as:

$$I_{stokes}(\nu) \propto \frac{(\omega_i - \omega_\nu)^4}{\omega_\nu} r_{\alpha\beta}(\nu); r_{\alpha\beta}(\nu) = |\frac{\partial \chi_{\alpha\beta}}{\partial U(\nu)}|^2 \tag{2.5}$$

where χ is the electric polarizibility of the system. Raman coefficients are third order derivatives of the energy that can be calculated using the (2n+1)-th theorem. There is another approach using DFPT+"frozen phonon": the dielectric tensor is calculated from DFPT with a phonon "frozen in" and then the derivation with respect to the phonon coordinate is done numerically.

2.8 Determination of Kinetic parameters for surface reactions

The best way to determine the kinetic parameters for a reaction would be to obtain them from experiments.[7] However, it is not always possible to zoom into the specific reaction sites or observe a specific reaction in an experimental setup. Theoretical methods are routinely applied in such cases. The primary quantity of interest is the rate constant for which one often uses the Arrhenius form $W = \nu exp\left[-\frac{E_{act}}{k_B T}\right]$ with W as the rate constant, E_{act} as the activation energy and ν as the prefactor. The prefactor and the activation barrier are assumed to be temperature independent. Using the master equation[7]

$$\frac{dP_\alpha}{dt} = \sum_{\beta} [W_{\alpha\beta} P_\beta - W_{\beta\alpha} P_\alpha]$$

Here, t is time, $\alpha$and β are the configurations of the adlayer, $P_\alpha$and $P_\beta$are their probabilities, $W_{\alpha\beta}$and $W_{\beta\alpha}$are the transition probabilities per unit time that specifies the rate at which the adlayer changes on the surface. It can be shown[7] that this master equation also leads to a rate equation

$$W = \frac{k_B T}{h} \frac{Q^\ddagger}{Q} exp\left[\frac{-E_{bar}}{k_B T}\right] \tag{2.6}$$

with T as the temperature, $k_B$as the Boltzmann constant and h as the Planck's constant. The Q's are the partition functions and $E_{bar}$is the height of the activation barrier. The exact expression for the partition functions are

$$Q^\ddagger = \int_{S_{\beta\alpha}} dS \int_{-\infty}^{\infty} \frac{dp_1 dp_2 .... dp_{i-1} dp_{i+1} ... dp_D}{h^{D-1}} exp\left[-\frac{H - E_{TS}}{k_B T}\right] \tag{2.7}$$

$$Q = \int_{R_\alpha} dq \int_{-\infty}^{\infty} \frac{dp}{h^D} exp\left[-\frac{H - E_{IS}}{k_B T}\right] \tag{2.8}$$

where q stands for all coordinates, p stands for all momenta, D is the number of degrees of freedom, and the integration is over the region $R_\alpha$in configuration space. H is the hamiltonian for the system, E_{IS} is the minimum of the potential energy in $R_\alpha$and E_{TS} refers to the minima on the saddle point $S_{\beta\alpha}$. Hence, the partition functions correspond to the initial and the transition state for a surface reaction. We also have $E_{bar} = E_{TS} - E_{IS}$.

2.8.1 Zero-point energy

A quantum mechanical partition function can be written as

$$Q = \sum_{n=0}^{\infty} exp\left[-\frac{E_n}{k_B T}\right] \tag{2.9}$$

with the summation over all eigenstates of the hamiltonian of the system.[7] When we define the state n=0 as the ground state, then this expression can be rewritten as

$$Q = exp\left[\frac{-E_o}{k_B T}\right] \sum_{n=0}^{\infty} exp\left[-\frac{E_n - E_0}{k_B T}\right]$$

The previous definitions of the partition functions[7] tells us that the energies of the states should be taken with respect to a minimum of the potential energy. The difference between this minimum $E_o$and this true minimum is known as the zero point energy. The equation (2.7) can also be written as

$$W = \frac{k_B T}{h} \frac{Q^{\ddagger}}{Q} exp\left[-\frac{E_{bar} + E_{ZPE}}{k_B T}\right] \tag{2.10}$$

where E_{ZPE} contains all the zero point energy corrections from the partition functions. We also have $E_{ZPE} = \varepsilon_{TS} - \varepsilon_{IS}$. The quantity $E_{bar} + E_{ZPE} = E_{act}$ which is also known as the zero-point energy corrected activation barrier or just the activation energy.

2.8.2 Vibrational partition function

The energies of the states in a quantum harmonic oscillator are given by $E_n = (n + \frac{1}{2})h\nu$ with n being a non-negative integer and starting from zero. The summation of the partition function (2.9) can be done analytically and the result for the partition function[7] is

$$Q_{vib} = Q^{\sim}_{vib} exp\left[\frac{-h\nu}{2k_B T}\right] \tag{2.11}$$

with $Q^{\sim}_{vib} = \frac{1}{1-exp\left[\frac{-h\nu}{k_B T}\right]}$. The quantity $exp\left[\frac{-h\nu}{2k_B T}\right]$ is a zero-point energy factor that can be later combined with $exp\left[\frac{-E_{bar}}{k_B T}\right]$. The value of the parition function $Q^{\sim}_{vib}$ can be approximated by 1 if $h\nu >> k_B T$ which is the usual case. Also, when $h\nu << k_B T$ we have $Q^{\sim}_{vib} = \frac{k_B T}{h\nu}$.

2.9 Nudged Elastic Band (NEB) method

In order to estimate the reaction rates, determination of the saddle point is extremely crucial. A path that connects the initial and final states and which typically has the greatest statistical weight is termed as the minimum energy pathway (MEP).[15] The maxima on the MEP are saddle points on the potential energy surface. Often the MEP may have more than one minima other than the initial and the final states. These usually correspond to stable intermediate states. Assuming a Boltzmann distribution for the population in the intermediate states, the overall rate would be determined by the highest energy saddle point. Methods for finding the saddle point involve maximization of one degree of freedom and minimization of the rest. The NEB has been shown to be an effective method to determine the MEP between a given set of optimized initial and final states. It has also been popular to estimate reaction rates using the hTST approximation. The method is employed along with plave wave-DFT to determine the forces acting on the images. The MEP is found by constructing a set of images between the initial and the final states. A spring interaction is added between the images to ensure that the path remains continuous, thus eventually resembling an elastic band.[15] An optimization of this band w.r.t the forces acting parallel and perpendicular to it would eventually make it sink to the MEP.

Within NEB[15], the force projections are adjusted in such a way that the spring force does not interfere with the convergence of the band to the MEP and the true force does not impact the distribution of the images along the MEP. The true force and the spring force are decomposed into components parallel and perpendicular to the path. Only the perpendicular component of the true force and the parallel component of the spring force are included. This is commonly referred to as 'nudging'.[15] The spring forces then control the spacing of the images along the band whereas the true force causes the images to slide down from the high energy regions towards the minima. The method is designed in such a way so as to eliminate any sort of competition between the forces, thus allowing the spring forces to be variable and different in orders of magnitude compared to the true forces.

2.9.1 Regular NEB

An elastic band[15] with N+1 images can be denoted by $[R_o, R_1.....R_N]$,where the end points $R_o$and R_N are fixed and determined according to the energy minima obtained after geometry optimization of the initial and final states. The N-1 intermediate images are optimized according to the algorithm. In the NEB method,[15] the total force acting on an intemediate image is the sum of the spring force along the local tangent and the perpendicular component of the true force

$$F_i = F_i^s \mid_{\parallel} -\nabla E(R_i) \mid_{\perp} \tag{2.12}$$

where the true force is given by $\nabla E(R_i) \mid_{\perp} = \nabla E(R_i) - \nabla E(R_i) \cdot \tau_i$; here E is the energy of the system, a function of all the atomic coordinates and evaluated using DFT; $\tau_i$is the normalized local tangent at image i. The spring force is

$$F_i^s \mid_{\parallel} = k(\mid R_{i+1} - R_i \mid - \mid R_i - R_{i-1} \mid)\tau_i \tag{2.13}$$

where k is the spring constant. An optimization algorithm is used to move images according to the force in equation (2.12). If the spring constant is kept fixed, all the

images are equally spaced from each other. Usually, none of the images land exactly at the saddle point. The location of the saddle point is then determined using an interpolation scheme.[15]

2.9.2 Climbing Image NEB

The Climbing image implementation[15] of NEB consists of a small modification to the regular NEB. Not only does it retain the entire shape of the MEP, it also ensures a rigorous convergence of an image to the exact saddle point. Also, it has been shown that this new modification does not increase the computational efforts and hence is very feasible to implement. After a few iterations with the regular NEB, the highest energy image i_{max} is identified. The force on this image is given by the new equation:

$$F_{i_{max}} = -\nabla E(R_{i_{max}}) + 2\nabla E(R_{i_{max}}) \mid_{\parallel} = -\nabla E(R_{i_{max}}) + 2\nabla E(R_{i_{max}}) \cdot \tau_{i_{max}} \tau_{i_{max}} \quad (2.14)$$

This is the full force according to the given potential with the component along the elastic band inverted. The spring forces do not affect the highest energy image which allows it(also called the climbing image) to move up the potential surface along the band and down the surface perpendicular to the band. The other images now serve the purpose of defining the only degree of freedom for which the maximization of the energy is carried out. As long as the Climbing image converges, it shall do so to the saddle point! There is no extra computational cost involved.[15] This method eliminates the need of an extrapolation across the saddle point as was required in the regular NEB method. It is quite robust and leads to the exact determination of a saddle point. In order to *increase* the resolution around the saddle point, the images around it can be brought closer to one another by implementing a *variable* elastic constants scheme. A stronger spring constant would bring the images closer and help in a more accurate determination of the tangent near the saddle point. The convergence of the elastic band to the MEP is *not* affected by using springs with different force constants. The force constant k is linearly scaled w.r.t energy such that the highest energy images are connected by the strongest springs.[15] Within Quantum Espresso, the neb.x package enables us to set a range $[k_{max}, k_{min}]$ for the force constants such that the images near the saddle point are connected by the k_{max} springs.

Chapter 3

Computational Methods

3.1 DFT method and model validation

3.1.1 The Slab model for the catalyst Co(0001) surface

Using Accelerys Materials Studio© 6.0, I modelled the Cobalt(0001) catalyst surface as a vacuum supercell. It was repeated periodically in all the three directions akin to a crystal structure. Slabs in neighbouring cells were separated by a *vacuum space* with a length of 20 Å along the z-direction. This was enough to accommodate all the adsorbate species present on the slab surface and to avoid inter-cell interactions in the z-direction. Depending on the type of calculation, the slab was either a p(4x4), p(3x3) (fig 3.1) or a p(2x2) 6-layer/4layer supercell where the notation p(4x4) implies that there are 16 atoms per layer. The bottom two layers were always kept fixed at the equilibrium Co bond distances. This represented the bulk metal.

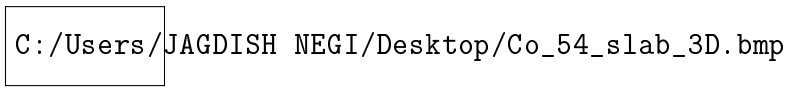

Figure 3.1: Supercells of 6-layered, p(3x3) Co vacuum slab extended two times in all three directions

The adsorbate species such as H and CO were placed at different sites (fig 3.2) on the surface and then the entire structure was allowed to relax under a certain force and total energy convergence criterion. The adsorbates moved around and finally settled to their most preferred adsorption site. These results were verified by comparing with data available from the literature.

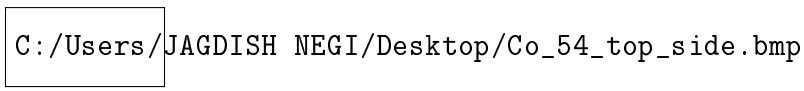

Figure 3.2: Adsorption sites shown on a p(3x3) Co vacuum slab surface(top view)

The coverage for these adsorbates was changed by using more number of atoms on the surface. The fractional coverage of a surface is defined by the quantity θ:

$$\theta = \frac{Number..of..occupied..adsorption..sites}{Total..number..of..possible..sites}$$

The adsorption energy for a particular adsorbate was calculated w.r.t it's gas phase using the follwing scheme:

$$E(ads) = \frac{[E(complex) - E(slab) - \{(n/i) \times E(molecule)\}]}{n}$$

where for a molecule such as H_2, i = 2 and n = number of atoms present on the surface or the subsurface of the Co vacuum slab and for a molecule such as CO, i = 1 and n = number of molecules adsorbed on the slab surface. This was formulated based on the experimental observation that Hydrogen adsorbs dissociatively on Co(0001) surface wheras CO adsorbs without undergoing dissociation.

3.1.2 Testing Pseudopotentials

For our study, we first needed to test various pseudopotentials. These were used to calculate properties of simple systems that were very well documented in the literature. The following molecules were used as test systems: CO, CO_2,CH_4 and $Co_2(CO)_8$. In order to determine the accuracy of the pseudopotentials, we have compared the calculated bond lengths and vibrational frequencies with those values that have been determined experimentally.

3.1.2.1 Bulk Cobalt

We needed a pseudopotential that was *ultrasoft* in nature, involved *nonlinear core correction,* was *non-relativistic* and made use of *PBE exchange correlational* functional. We chose Co.pbe-nd-rrkjus which was generated using the Andrea Dal Corso code (rrkj3) and satisfied all our requirements. Co had been known to exist in two crystal phases: FCC and HCP. It had been shown experimentally that at room temperature Co has a HCP structure. We tried to validate this by calculating the zero kelvin energy of bulk Co. The HCP structure was expected to have a lower energy than the FCC. The calculations were done using an 8-atom supercell. The energies have been plotted w.r.t the k-point sampling (using Monkhorst-Pack grids) of the brillouin zone and the kinetic energy cut-off. Table 3.1 lists the results w.r.t k-point sampling. The kinetic energy cut off for these runs was set at 450 eV.

k-points	Energy (eV), HCP	Energy (eV), FCC	ΔE (HCP-FCC)(eV)	Magnetic moment/atom (BM) , FCC	Magnetic moment/atom (BM), HCP
6x6x6	-8096.41	-8096.01	-0.40	1.77	1.84
9x9x9	-8096.44	-8096.05	-0.39	1.76	1.81
12x12x12	-8096.44	-8096.04	-0.40	1.76	1.82

Table 3.1: Energies of HCP vs FCC for bulk Cobalt

Continuing ahead, the energies of both the structures were calculated at different kinetic energy cut-offs. The k-point sampling was done using a Monkhorst-Pack grid of dimensions 12x12x12. For each ecutwfc, we could see (Table 3.2) that the HCP structure again had a *lower* energy compared to the FCC structure.

Kinetic Energy cut off (eV)	Energy (eV) HCP	Energy (eV) FCC	ΔE /eV (HCP-FCC)	Magnetic moment/atom (BM), HCP	Magnetic moment/atom (BM), FCC
450	-8096.45	-8096.04	-0.41	1.82	1.76
425	-8096.42	-8096.01	-0.41	1.82	1.76
400	-8096.41	-8095.99	-0.42	1.82	1.76

Table 3.2: Energies and Magnetic moments at different kinetic energy cut-offs for FCC and HCP Cobalt

As reported in the literature the experimental magnetic moment/atom for Cobalt was around 1.7 μ_B. This agreed well with our calculations which yielded magnetic moments consistently around 1.8μ_B. The experimental bond length for Co was reported to be 2.506 Å. From our calculations, the average bond length for the HCP supercell comes out to be 2.51 Å and for the FCC supercell, it comes out as 2.45 Å. The HCP bond length was in good agreement with the literature values. Also, the energy of the HCP structure was consistently lower than the FCC. Under Fischer-Tropsch conditions, it had been already shown that Co largely retains the HCP structure. Hence, we decided to use this for building a vacuum slab that would act as a model for the catalyst surface.

3.1.2.2 Carbon monoxide

The bond length calculations have been summarized in the following Table 3.3

PP[C]	PP[O]	Our result/bond length (Å)	Expt bond length (Å)
C.pbe-rrkjus.UPF	O.pbe-rrkjus.UPF	1.141	1.128
C.pbe-van_ak.UPF	O.pbe-van_ak.UPF	1.144	
C.pbe-van_bm.UPF	O.pbe-van_bm.UPF	1.142	

Table 3.3: Bond length calculations for CO

The pseudopotentials in the first row gave the bond length that were closest to the experimental value. Using this set of PP, the vibrational spectra of CO was calculated. The PHonon 5.0.1 package in QE was used to calculate the frequency of oscillation of an isolated CO molecule which could later be compared with the experimental gas phase CO infrared vibrational data. The literature value[13] of C-O frequency is 2143 cm^{-1}. Using the PHonon 5.0.1 package we obtained an IR active mode with a frequency 2103.58 cm^{-1} and an intensity of 1.4128 $debye^2/Å^2amu$. The result was considered to be in fairly good agreement with the literature value.

3.1.2.3 Carbon dioxide

Bond lengths calculated using the pseudopotentials based on the Andrea Dal Corso code (rrkj3) were closest to the experimental values. These are then used to determine the vibrational spectra for the molecule. Using the PHonon 5.0.1 package, a vibrational calculation was done on an isolated CO_2 molecule.

The phonons were calculated at the wavevector q(0,0,0). Both the *acoustic sum rule* and *symmetry* were used to reduce the number of calculations to the strict minimun! It was also seen that the symmetry of a molecule in a supercell was necessarily a subgroup of the lattice symmetry and hence lower than the true molecular symmetry. This resulted in the spreading of the degenerate vibrational levels. The auxiliary program dynmat.x read the files produced by ph.x and applied various forms of Acoustic sum rule (ASR) to calculate the IR cross sections. The obtained frequencies and the IR intensities have been listed in Table 3.4

Vibrational modes	Our results/QE (cm^{-1})	All electron (cm^{-1})[1][2]	IR intensity($D^2/Å^2$- amu)
O-C-O bend	640.51	641.49	0.5036
O-C-O bend	641.06	641.49	0.5043
C-O symmetric stretch	1300.79	1373.01	0.0002
C-O asymmetric stretch	2334.46	2438.1	11.9587

Table 3.4: Vibrational modes for CO_2using DFPT

3.1.2.4 Methane

The molecule consists of the species C and H. The input geometry was made using Materials Studio 6.1 and the molecule was relaxed using stringent convergence criterion. The bond lengths from the relaxed structures were then compared with the literature values. Once again the rrkj3 pseudopotentials gave the most accurate results. The vibrational calculations were done at a single wavevector q(0,0,0). The results were then compared with the known all electron vibrational modes as shown in Table 3.5

Mode	Our results/QE (cm^{-1})	All electron (cm^{-1})[1][2]	IR intensity ($D^2/Å^2$-amu)
Bending	1284.49	1375.75	0.3176
Bending	1284.64	1375.75	0.3198
Bending	1285.96	1375.75	0.3189
Twisting	1506.91	1597.55	0.000
Twisting	1508.16	1597.55	0.000
Symmetric stretch	2965.97	3054.37	0.000
Asymmetric stretch	3084.00	3167.12	0.4248
Asymmetric stretch	3084.46	3167.12	0.4245
Asymmetric stretch	3084.85	3167.12	0.4232

Table 3.5: Vibrational modes for CH_4 using DFPT

The PHonon/QE results matched reasonably with the all electron values. The reduced symmetry of the system introduced some spread in the otherwise degenerate vibrational modes. Also, the lowest energy modes were the most underestimated by the pseudopotential approach. The results obtained here seemed to match and in some cases were better than those documented by [20].

3.1.2.5 Dicobalt Octacarbonyl $Co_2(CO)_8$

This metal carbonyl is a popular reagent and also a catalyst in organometallic chemistry and organic synthesis. It serves as an useful model system as it captures the interaction between CO and cobalt and also being a small system, it would not require long computational time to test our pseudopotentials. The pseudopotentials that had given the best results for the earlier three test molecules were used to determine the bond lengths and the vibrational spectra of all the three isomers of $Co_2(CO)_8$. The results were compared from similar studies[21] done using basis sets that employed contracted gaussian functions. We followed the work of [21] where they had done DFT based studies using three-parameter Becke exchange functional with the Lee-Yang-Parr nonlocal correlational functional known as B3LYP and also another DFT method, which combined Becke's 1988 exchange functional with Perdew's 1986 nonlocal correlational functional (BP86).

The input geometries for the three symmetries were made using Material Studio 6.0. The bond lengths were adjusted to be close to the particular symmetry considered. Each of the three $Co_2(CO)_8$structures was expected to be a genuine minima over the entire potential energy surface. Hence, the geometry we attained finally depended on the minima closest to which we started with.

1) Dibridged $Co_2(CO)_8$with C_{2v} symmetry - The structure was optimized with stringent relaxation criterion. The scf convergence criterion was set at 10^{-6}eV/atom, the max. displacement for geometry optimization was set to 0.002 Å the maximum force is 0.05 eV/Å and the ionic energy convergence was set to 2 x 10^{-5}eV/atom. The calculations were done at the gamma point. The bond lengths from the relaxed structure were compared (see Table 3.6) with that obtained using the B3LYP and BP86 DFT methods.[21]

Bond type	B3LYP (Å)	BP86 (Å)	Our result/QE (Å)	Expt Bond length (Å)
Co-Co	2.557	2.550	2.539	2.528
Bridge C-O	1.176	1.188	1.176	1.167
Co-C terminal(1)	1.827	1.813	1.799	1.827
Co-C above bridge(2)	1.820	1.805	1.794	1.827
C-O terminal (3)	1.151	1.166	1.153	1.136
C-O above bridge (4)	1.152	1.166	1.153	1.136

Table 3.6: Comparison of bond lengths for $Co_2(CO)_8$ with C_{2v} w.r.t different basis sets

The Co-Co bond length estimated using PWscf/QE was in very good agreement with the experimental data. It had given a better estimate compared to the other two DFT methods. A snapshot of the relaxed C_{2v} structure obtained using Xcrysden 1.5.24 is shown in fig 3.3

All the 54 vibrational modes were calculated using DFPT as implemented in QE and matched with the results published by Kenny et al[21] using different basis sets. Almost all our results matched very well and in some cases turned out to be better than those predicted by Kenny et al.[21]

2) Unbridged $Co_2(CO)_8$ with D_{3d} symmetry - This geometry exists in equilibrium with the C_{2v} structure in a solution. It was considered to be the minor isomer and both the forms would rapidly interconvert! The input structure was built using Material Studio 6.1. The bond lengths were kept close to that of the D_{3d} symmetry so that upon

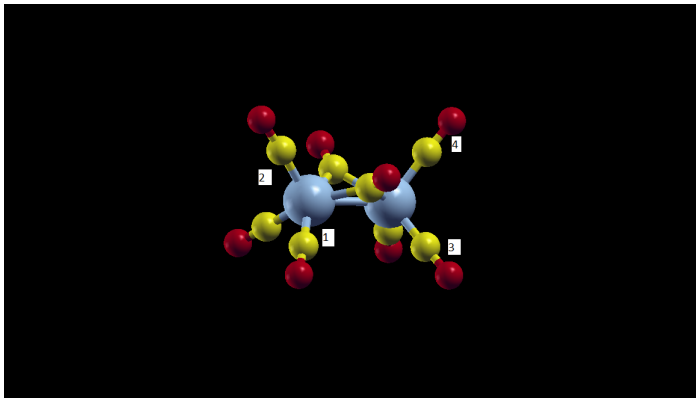

Figure 3.3: Relaxed C_{2v} structure of $Co_2(CO)_8$showing the different bond types

relaxation the molecule goes to this particular minima. The convergence criterion for geometry relaxation was similar to that of the C_{2v} structure. The bond lengths from the relaxed structure were compared (Table 3.7) with those obtained from B3LYP and BP86 DFT methods.[21]

Bond type	B3LYP (Å)	BP86 (Å)	Our results/QE (Å)
Co-Co	2.721	2.692	2.689
C-O end terminal (1)	1.152	1.167	1.155
Co-C end terminal (2)	1.783	1.767	1.799
Co-C trigonal (3)	1.817	1.808	1.856
C-O trigonal (4)	1.154	1.168	1.155

Table 3.7: Comparison of bond lengths for $Co_2(CO)_8$with D_{3d} symmetry using different basis sets

The bond lengths were in fairly good agreement with those obtained from other DFT methods. A snapshot of the relaxed D_{3d} structure obtained using Xcrysden is as follows: (figure) Red-O, Yellow-C, Blue- Co

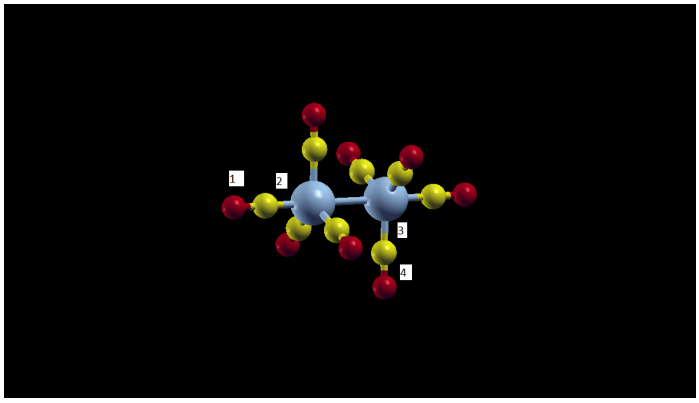

Figure 3.4: Relaxed D_{3d} of $Co_2(CO)_8$ structure showing different bond types

Vibrational analysis using DFPT again gave results that matched very well with the works of Kenny et al.[21]

3) Unbridged $Co_2(CO)_8$ with D_{2d} symmetry - This structure had been proposed based on certain IR vibrational experiments. The structure had not been optimized before until the work of Brienne et al.[23] The bond lengths from the relaxed structure obtained using plane waves in QE were compared (Table 3.8) with the other mentioned DFT methods.

Bond type	B3LYP (Å)	BP86 (Å)	Our results/QE (Å)
Co-Co	2.666	2.629	2.866
Co-C terminal Left (1)	1.799	1.793	1.799
Co-C terminal Right (2)	1.812	1.798	1.797
C-O terminal Left (3)	1.156	1.17	1.156
C-O terminal Right (4)	1.153	1.167	1.156

Table 3.8: Comparison of bond lengths for $Co_2(CO)_8$with D_{2d} symmetry using different basis sets

The converged structure was symmetric as the left and right Co-C and C-O bond lengths are the same. Except the Co-Co bond length, almost all others obtained using PWscf/QE were in good agreement with other DFT methods. A snapshot of the relaxed molecule obtained using Xcrysden-1.5.24 is shown in fig 3.5

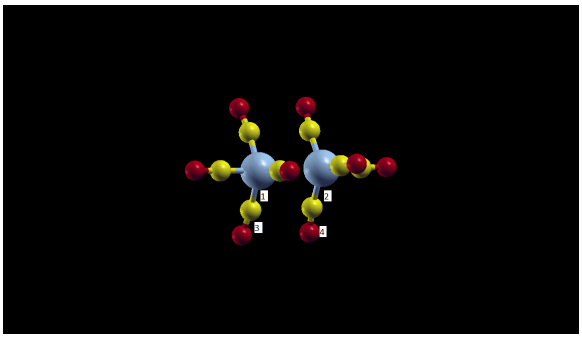

Figure 3.5: Relaxed D_{2d} structure of $Co_2(CO)_8$showing different bond types

All the 54 modes of this system were calculated using DFPT. The IR intensities were computed using the dynmat.x auxiliary program. The results have been compared with those obtained using other DFT methods[21] and were again found to be in good agreement.

Based on all the results the pseudopotentials that seemed to give the most accurate values were **Co.pbe-nd-rrkjus, C.pbe-rrkjus.UPF, O.pbe-rrkjus.UPF** and **H.pbe-rrkjus.UPF**. All these were constructed using Adrea Dal Corso code (rrkj3). These are ultrasoft, non-relativistic, involved nonlinear core correction and PBE exchange correlational functional. Ultrasoft pseudopotentials were also known to have a good transferability and hence were expected to give fairly accurate results for the Co vacuum slab geometry with adsorbed CO and H species.

3.1.3 Validation of parameters for the vacuum slab model

3.1.3.1 CO adsorption at $\theta = 0.25$

The validation was carried out by comparing the results obtained by plane-wave based DFT calculations on a p(4x4), 6-layer Co slab with those observed in experiments. We had mainly focused on determining the favourable adsorption sites for CO and H.

Site	d(OC—M)/Å	d(O—CM)/Å	E(ads) per CO/eV	E*(ads) per CO/eV
hcp	1.97	1.19	-1.67	-1.11
Bridge	1.88	1.18	unstable	unstable
Atop	1.74	1.16	-1.65	-1.26
fcc	1.98	1.19	-1.67	-1.11

Table 3.9: CO adsorption sites and energies at $\theta = 0.25$, CO prefers to adsorb at the atop site since it has the most negative adsorption energy

CO adsorption at a low coverage of $\theta = 0.25$ was studied for four different sites (see Table 3.9) on the surface of hcp Co(0001). As pointed out by Mason[25] , DFT tends to overestimate the CO adsorption energies. We had used the Mason correction scheme[25] on our data and reported the final corrected adsorption energy values in the last column of fig 4.18. Corrected energy **E*(ads)** = E(ads) + ΔE where ΔE is the empirical correction to the adsorption energy suggested by Mason and co-workers;[25] ΔE = A-B·ν where A = 1.996 eV and B = 0.0008 eVcm. The vibrational frequency $\nu(cm^{-1})$ is related to the C—O bond length d(Å) by the following relation [ν = 10203.2 – 7066.d].[26] After applying the *overbinding correction*, it was seen that CO preferentially adsorbs in the *upright atop* site which was in good agreement with the experimental results.[27]

3.1.3.2 H adsorption at $\theta = 0.25$

It was already well established that H adsorbs dissociatively on Co(0001) surface during FT synthesis. The adsorption was thus studied on a p(4x4), 6-layer Co vacuum slab at four different possible sites on the surface.

site	E(ads)/H in eV(w.r.t H_2)- our results!	E(ads)/H in eV (w.r.t H_2) [Helden; ACS Catalysis, 2012]
Atop	unstable	unstable
Bridge	unstable	-0.36
fcc	-0.54	-0.48
hcp	-0.51	-0.46

Table 3.10: H adsorption sites and energies at $\theta = 0.25$

The adsorption energy was calculated (see Table 3.10) as E(ads per H) = (1/x)*[E(ads/complex) – E(ads/slab) – (x/2)*E(H2)] where x was the number of H atoms. Based on the DFT energies, it could be inferred that H preferentially adsorbed on the fcc and hcp sites. This was again in good agreement with other theoretical[28] and experimental observations.

3.1.3.3 k-point sampling for the slab with adsorbate H-fcc and H-hcp

The calculations were again done on a p(4x4), 6-layer Co vacuum slab. The maximum change in the adsorption energy w.r.t k-point sampling(till a grid 6x6x1) was of the order ~ 0.06 eV. This was very less compared to the changes ($\tilde{}$ 0.1 eV) we need to see in order to make reliable qualitative predictions. Hence, we inferred that we need not sample the BZ at a higher k-point density than 3x3x1.

3.1.3.4 Effect of number of layers on the stability of subsurface H at $\theta = 0.25$

The number of layers for the p(4x4) Co vacuum slab was increased to 8 and it's effect on the subsurface H adsorption energies was studied. There was no appreciable change in the adsorption energy w.r.t the number of layers used and hence our slab model parameters involving 6 layers was very well suited to carry out further calculations!

3.1.3.5 Methyl adsorption on slab with subsurface H at $\theta = 0.25$

Again, we used a p(4x4), 6-layered Co vacuum slab to determine the preferential adorption sites for a methyl group w.r.t subsurface hydrogen. Based on the adsorption energy values, it was inferred that CH_3 prefers to sit at the hcp/fcc w.r.t subsurface hydrogen. The energies seemed to be of the same order as observed for methyl adsorption on Ni(111) with a monolayer of subsurface H.[8] Thus, we were able to correctly predict the adsorption sites for CH_3 based on it's chemisorption energies.

3.1.3.6 Slab model at realistic CO coverage of $\theta = 1/3$

The $\theta = 1/3$ coverage with the $(\sqrt{3} \times \sqrt{3})R30^o$ overlayer was modeled using a **p(3x3) 6-layer slab with 20 Å of vacuum along the z-axis.** Calculations with a smaller p(2x2) supercell had shown that adsorption energies show almost *negligible* change w.r.t supercell size provided that the coverage is same! Hence, we expected that the method and model parameters that we had verified earlier for the test systems should give accurate results for this realistic slab model too. However, we did repeat all our calculations for the p(3x3) model to ensure fair comparison of the final results.

CO site	d(OC−Co)/Å	d(O−CCo)/Å	E(ads) per CO /eV	E*(ads) per CO /eV
atop	1.75	1.16	-1.62	-1.21
bridge	*unstable	*unstable		
fcc	1.98	1.19	-1.61	-1.05
hcp	*unstable	*unstable		

Figure 3.6: Bond lengths and corrected adsorption energies[E*] for CO at a realistic coverage of $\theta = 1/3$

- As seen in fig 3.7, CO preferentially adsorbed in the upright atop position at a coverage $\theta = 1/3$ forming the $(\sqrt{3}\times\sqrt{3})R30^o$ overlayer. This was in good agreement with experimental LEED[27] observations at high CO pressures. Mason's correction[25]

(a) Top view (b) Side view

Figure 3.7: $(\sqrt{3} \times \sqrt{3})R30^o$ adsorbate coverage for CO at $\theta = 1/3$ on a p(3x3), 6-layered Co Vacuum slab

(also see sub-section 3.1.4.1) had been applied to compensate for the overestimation of the adsorption energy due to DFT.

- Conclusion: Our results for the d(O—CM) and d(OC—M) on the atop and fcc sites *matched well* with experimental studies: d(OC—Co)=1.78 +/- 0.06 Å and d(O—CCo)=1.16 Å.[27,29]

3.2 Normal mode analysis using DFPT implemented in PHonon/ph.x

The vibrational calculation[3] was started from a scf run that was done on the optimized structure at a particular adsorbate coverage. After obtaining the necessary wavefunction (.wfc) files the ph.x code[3] was initiated which read the input parameters from the &inputph namelist. For the Cobalt vacuum slab, the oscillations of the adsorbates might be coupled to that of the lattice. To verify if this were true, the normal mode analysis included some of the nearby Co atoms along with the adsorbed molecules. A big change in the primary adsorbate IR frequency would have indicated a strong coupling with the lattice. The normal mode analysis was also useful to do zero point energy corrections to the calculated activation barriers involving Hydrogen. The presence of an imaginary frequency for the transition state also helped to confirm that it was most likely a first order saddle point. Using *harmonic transition state theory,* the prefactor for methanation reactions was estimated[7] from the set of normal mode frequencies calculated for the corresponding reactants and products.

3.3 Transition State search using the Climbing Image - Nudged Elastic Band method implemented in PWneb / neb.x

The transition state search was carried out using the Nudged Elastic Band (NEB) method[15] which required the optimized structures of the reactants and products as the primary input. The path between the reactants and the products was connected by a discrete set

of images obtained using linear extrapolation. This path was then optimized according to the error constraint in the forces acting orthogonal to it. The objective here was to determine the minimum energy pathway (MEP) between the two primary images. The choice of the number of images in the path was governed by the trade off between accuracy in the determination of the activation barrier and the computational time. For most of our calculations, the total number of images was either set to 12 or 8. These particular numbers were chosen so that image parallelization within neb.x/QE[3] could be used to the full extent. Since the *-nimage* flag in the input script was set to 4, the number of images were restricted to be it's multiples i.e 8,12,16 etc. A literature survey revealed that an image number close to 10 was generally good enough to merit a comparison with experimental data. The calculation was started with a general NEB method and was allowed to run until the error dropped down to 0.5 eV/Å after which it was stopped and restarted with the *Climbing Image* option[15] enabled. The variable spring constants scheme was applied to have a higher resolution around the saddle point whenever the total number of images was set to a lesser value of eight! The images were evaluated at a k-point grid of 3x3x1 which was good enough as the energy estimates were accurate upto 10 kJ/mol compared to a 4x4x1 grid usually employed for geometry optimizations. This further helped to *reduce* the total computational time. The parameter path_thr determines the convergence w.r.t the error in the norm of the force orthogonal to the path in the units of eV/Å. Once the Climbing image mode was enabled, convergence upto 0.07 eV/Å was obtained within 200 iterations. The optimization scheme was set to 'broyden' which removed problems related to oscillations in the calculated activation energies.

Chapter 4

Results

4.1 Stability of surface and subsurface hydrogen at different coverages in the presence of CO at $\theta = 1/3$

The realistic CO coverage with $\theta = 1/3$ and $(\sqrt{3} \times \sqrt{3})R30^o$ overlayer structure was modeled using a p(3x3), 6-layered Co vacuum slab. The adsorption energy of surface and subsurface hydrogen (upto 3 sublayers) was calculated as described in section 3.1.2. Since the sublayer hydrogen is less stable compared to the surface hydrogen, the adsorption energies were expected to be positive. However, at the Fischer-Tropsch reaction temperature and pressure conditions (T $\sim$ 500K and pressures upto 10 bar) subsurface hydrogen becomes stable as shown previously.[4] Our aim here was to study the effect of surface CO on the DFT 0K adsorption energies of surface and subsurface hydrogen.

4.1.1 H at $\theta = 0.11$ in the presence of CO at $\theta = 1/3$

The surface coverage was realized by placing one hydrogen atom on the fcc site of a Co(0001) slab surface as shown in fig 3.2. The realistic CO coverage was modeled as shown in fig 3.7. The adsorption energy was calculated by the procedure that was described in section 3.1.1.

Site	Sublayer	E(ads) per H (eV) without CO	E(ads) per H (eV) with CO
Surface/fcc	--	-0.54	-0.44
Octahedral void	1	0.18	0.12
	2	0.03	0.07
	3	0.07	0.10

Table 4.1: DFT based adsorption energies of H at $\theta = 0.11$ in the p(3x3), 6-layered Co(0001) vacuum supercell

- From Table 4.1, we could see that presence of CO decreases the stability of surface hydrogen (since adsorption energy is less negative). This would have happened most likely due to repulsion from the adsorbed CO molecules. We had expected the effect to be more pronounced at higher hydrogen coverage.

- Stability of hydrogen in the first sublayer increased (became less positive!) in the presence of CO at realistic coverage. However, the change was within the DFT error limits (~ 0.1 eV) and further study was warranted before drawing any major conclusions.

4.1.2 H at $\theta = 0.22$ in the presence of CO at $\theta = 1/3$

Site	Sublayer	E(ads) per H (eV) without CO	E(ads) per H (eV) with CO
Surface/fcc	--	-0.55	-0.32
Octahedral void	1	0.21	0.12
	2	0.06	0.08
	3	0.10	0.10

Table 4.2: DFT based adsorption energies of H at $\theta = 0.22$ in the p(3x3), 6-layered Co(0001) vacuum supercell

- From Table 4.2, we could see that presence of CO further *reduces* the stability of surface hydrogen.
- The stability of hydrogen within the first sublayer seemed to increase (becomes less positive) but the values were still within the DFT error range, hence rendering any definite prediction difficult!
- Since there was very little or no change in the DFT based adsorption energies for subsurface hydrogen within the second and third sublayers, we concluded that they were *not affected* by the presence of CO.

4.1.3 H at $\theta = 0.33$ in the presence of CO at $\theta = 1/3$

Site	Sublayer	E(ads) per H (eV) without CO	E(ads) per H (eV) with CO
Surface/fcc	--	-0.55	-0.23
Octahedral void	1	0.22	0.13
	2	0.07	0.09
	3	0.10	0.11

Table 4.3: DFT based adsorption energies of H at $\theta = 0.33$ in the p(3x3), 6-layered Co(0001) vacuum supercell

- From Table 4.3, we can clearly see the trend in the reduction of stability for surface hydrogen at higher coverages.

4.1.4 H at $\theta = 0.44$ in the presence of CO at $\theta = 1/3$

Site	Sublayer	E(ads) per H (eV) without CO	E(ads) per H (eV) with CO
Surface/fcc	--	-0.52	-0.08
Octahedral void	1	0.20	0.11
	2	0.06	0.08
	3	0.09	0.09

Table 4.4: DFT based adsorption energies of H at $\theta = 0.44$ in the p(3x3), 6-layered Co(0001) vacuum supercell

4.1.5 Summary

As can be seen from fig 4.1, the surface hydrogen adsorption energy becomes less negative in the presence of CO (at $\theta = 1/3$) with increasing hydrogen coverage whereas it remains more or less *unchanged* in the absence of CO. This implies that surface hydrogen stability *decreases* in the presence of CO as its coverage approaches $\theta = 0.50$. From earlier works,[28] it can be inferred that the saturation coverage for surface hydrogen adsorption most likely lies close to $\theta = 0.50$. Further hydrogen adsorption on the surface is kinetically hindered! Since the surface hydrogen seems to become less stable in the presence of CO close to the hydrogen saturation coverage, it is more likely to *diffuse* into the subsurface further providing evidence that at Fischer-Tropsch conditions, subsurface hydrogen might have a major role to play in the process of methanation.

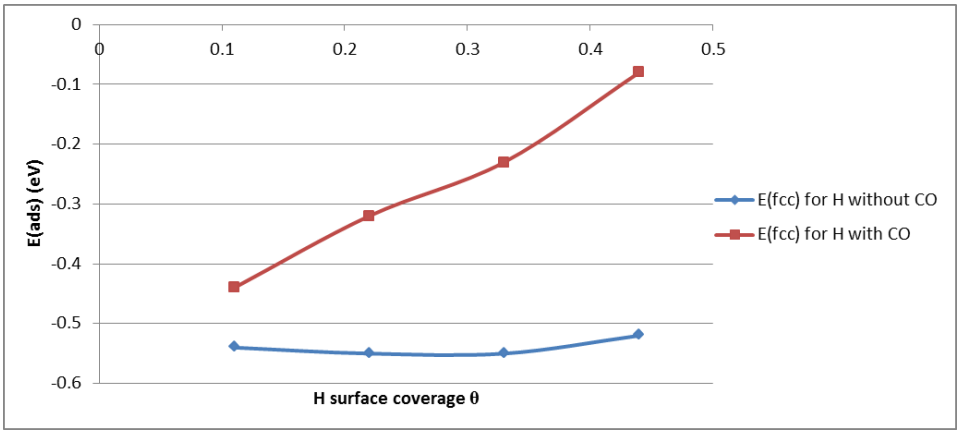

Figure 4.1: Variation in adsorption energy of H at surface fcc sites w.r.t coverage θ for Co(0001) surface

The graph in figure 4.2 indicates that hydrogen in the first sublayer *does not* seem to interact much with the adsorbed CO molecules. The difference between the energies in the absence and the presence of CO at different θ is fairly constant and well within DFT prediction error of ~ 0.1 eV. Also, we had seen from Tables 4.1 to 4.4 that going further down, adsorption energies for hydrogen in sublayers 2 and 3 were almost unchanged in the presence of CO. This observation could be attributed to the fact that the distance

between these hydrogen atoms and the surface CO groups was quite large, thus lowering any sort of interactions. Hence, based on the earlier work[4] and the above discussed results, we can argue that at Fischer-Tropsch reaction conditions, even in the presence of surface CO groups, subsurface hydrogen would still exist and for certain coverages would be stable. Since CO does not alter the hydrogen adsorption energies, we decided to conduct the computationally intensive transition state search calculations for different methanation pathways on a clean Co(0001) surface in the absence of CO.

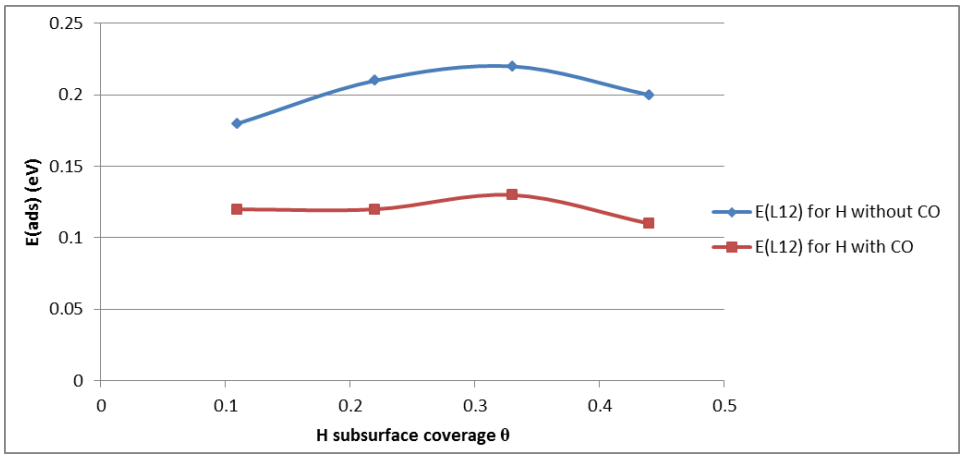

Figure 4.2: Variation in adsorption energy of H within the first sublayer w.r.t coverage θ for Co(0001) surface

4.2 Transition state search using the Nudged Elastic Band (NEB) method

4.2.1 H_2 dissociation on a clean Co(0001) surface

The calculations for the dissociation of an isolated hydrogen molecule were done on a 4-layered p(3x3) Co vacuum slab. The parameters were chosen as described in section 3.3 in the previous chapter. Here, the H_2molecule starts at a distance of $\sim$ 4Å above the surface in a p(3x3), 4-layered Co(0001) slab. As the molecule comes closer to the surface the energy changes have been recorded in fig 4.3.

The initial energy has been rescaled to zero and all the subsequent changes are w.r.t this reference. The minimum energy pathway (MEP) has the H_2molecule dissociating over the top site after which the atoms settle into the fcc voids on the surface. Following this pathway, we can see that initially the energy of the system increases and reaches a maximum value of 0.05eV at a distance of about 2.5 Å. After this barrier has been crossed, the energy decreases to a minimum at about 1.9 Å. From this minimum, only a small energy $\sim$0.02 eV is required to dissociate the H_2 molecule at a distance of 1.5 Å. This profile matches quite accurately with that obtained by Helden et al[28] for H_2dissociation on Co(111) surface. Since it has been shown that the adsorption energetics on Co(111) are very similar to Co(0001), this result *successfully validates* our NEB method parameters.

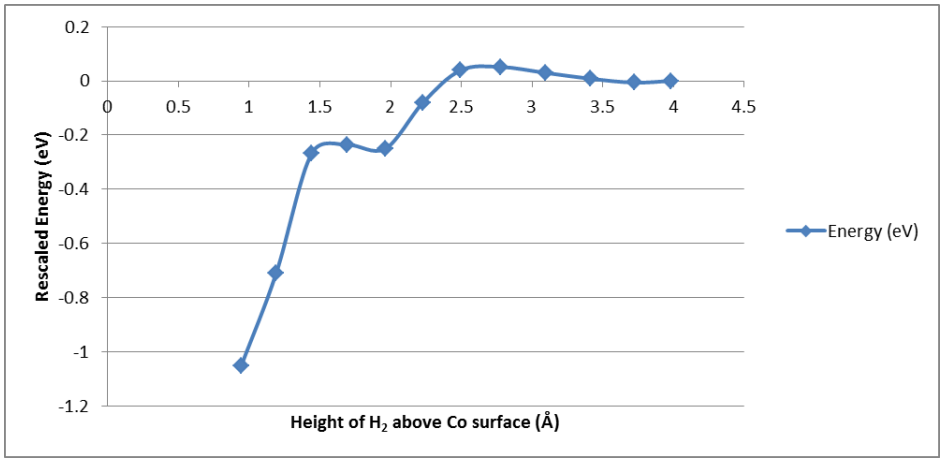

Figure 4.3: Minimum energy pathway for H_2 dissociation on a clean Co(0001) surface; Data points on the blue curve correspond to images of Co vacuum supercell structures where the rightmost image contains a H_2molecule adsorbed at a distance of 4 Å. As we move left on the X-axis(reaction coordinate), the H_2molecule approaches the slab surface and dissociates with the H atoms adsorbed on the fcc sites(see chapter-3, fig 3.2).

4.2.2 H_2 diffusion into the first sublayer

The calculations for the diffusion of hydrogen atoms into the first sublayer were done on a 4-layered p(3x3) Co vacuum slab. As can be seen from the MEP in fig 4.32, hydrogen within the first sublayer is about 1.5 eV higher in energy compared to the surface. The barrier for diffusion into the subsurface is quite high at about 1.8 eV. However, it requires only about 0.3 eV to drive a subsurface H atom onto the surface. Earlier in-house studies have proven that the energetics of this diffusion towards the subsurface site will highly depend on the hydrogen coverage.[4] At higher coverage of hydrogen, it would become more favorable for hydrogen to diffuse towards the subsurface sites.

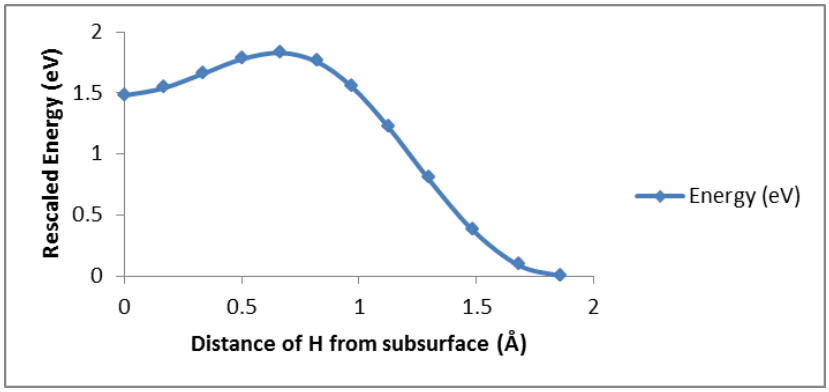

Figure 4.4: Minimum energy pathway for hydrogen diffusion into the first sublayer in Co(0001); The reaction coordinate is defined as the distance of the H atoms from the first sublayer, hence the H atoms start from the surface at a distance of 1.8 Å and gradually move (left on the X-axis) towards the sublayer. The value of 0 Å corresponds to the H being in between the Co(0001) surface and the first Co sublayer.

4.2.3 Methanation pathway-1

The transition state search for pathway-1 was carried out on a p(2x2), 6-layered Co vacuum slab model. It had already been verified that the adsorption energies for the methyl group were similar (within 0.05 eV) to those obtained using the larger p(4x4), 6-layered slabs at the same coverage. Knowing that NEB calculations take very long times to converge, we opted for the former smaller system for our future calculations. The initial reactant structure for this calculation consisted of a hydrogen atom in an octahedral void within the first sublayer and a methyl group adsorbed at a surface hcp site adjacent to the hydrogen.

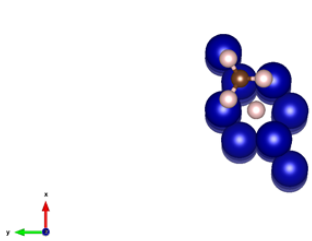

(a) Top view of Co(0001) surface with subsurface H atom and methyl group chemisorbed at an adjacent surface hcp site

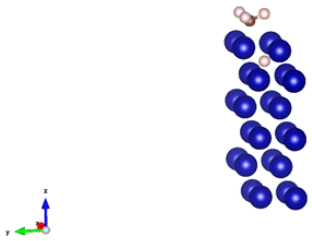

(b) Side view of Co(0001) surface with subsurface H atom and methyl group chemisorbed at an adjacent surface hcp site

Figure 4.5: Initial reactant structure for pathway-1 on a p(2x2), 6-layered Co vacuum supercell, Blue-Co atoms, White-Hydrogen, Grey-Carbon

The product structure (fig 4.6) consists of a methane molecule physisorbed at a distance of ∼4 Å from the Co surface.

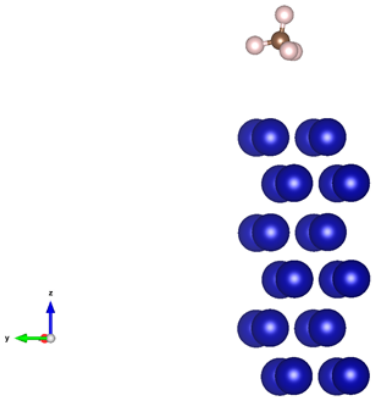

Figure 4.6: Product structure for pathway-1, Blue-Co atoms, White-Hydrogen, Grey-Carbon

At first, the NEB was run at a coarse convergence criterion without implementing the Climbing-Image scheme. An intial analysis of the MEP in fig 4.7 showed the existence of two transition states which were suspected to be a resurfacing and a recombination barrier for hydrogen. There seemed to be no evidence of a direct pathway for methane formation

starting from this configuration. The subsurface hydrogen resurfaced at a fcc site close to the methyl group. It was followed by the recombination event. To accurately determine the activation barriers, the entire path was split into two separate NEB calculations.

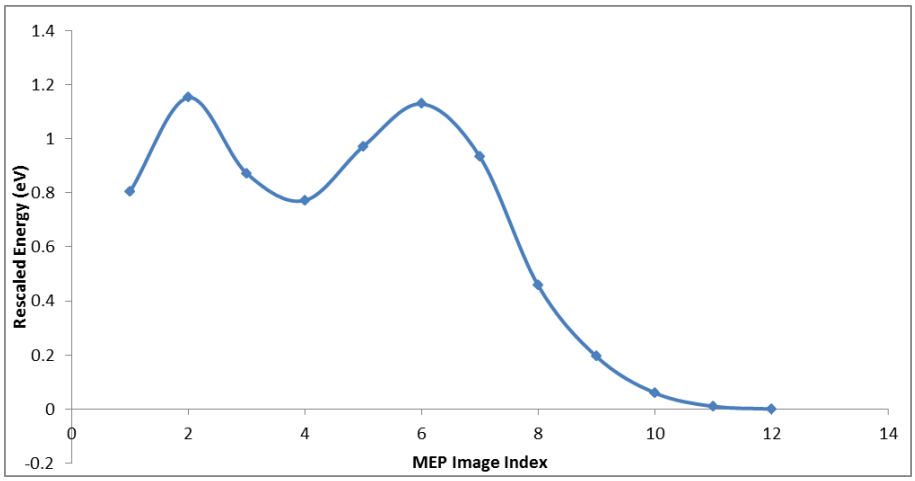

Figure 4.7: Rescaled energy vs the image index for the full pathway-1; image index # 1 corresponds to the initial reactant structure as shown in fig 4.5 whereas the image index # 12 corresponds to the final product structure as shown in fig 4.6; Energies have been rescaled such that the product structure(with methane as in fig 4.6) is at 0 eV.

The Transition state for the resurfacing event was converged to an accuracy of 0.02 eV/Å and the recombination event to an accuracy of 0.05 eV/Å. The zero point energy (ZPE) corrected barriers for both the transition states are listed in the figures itself.

The transition states for both the resurfacing and the recombination events as shown in figs 4.8 and 4.9 respectively were verified by conducting a normal mode analysis using DFPT as implemented in Quantum Espresso(see Chapter 3, Section 3.2). Since a transition state is a first-order saddle point, the reactive hydrogen has exactly one imaginary frequency. In our case, the frequency corresponding to the displacement of the reactive hydrogen in the *z-direction* was imaginary which confirmed that the *highest energy image had indeed converged to a saddle point.* As discussed by Michaelides et al,[6] if the coordination number of the site where an adsorbate has chemisorbed (CH_3 adsorbed at surface hcp site in our case) is greater than it's valency, then in order to form a transition state, it must move to a site of *lower coordination.* Analysis of the transition state geometry (see appendix B.1) for the recombination event as shown in fig 4.9 revealed that the methyl group (valency = 1) has moved from the surface hcp site (Coordination number = 3) to the top of a nearby Co atom which is the atop site (coordination number = 1). Hence, our observations are consistent with a well known generalized framework[6] developed for microscopic reaction pathways in heterogeneous catalysis which further validates the accuracy and robustness of our NEB calculations.

4.2.4 Methanation Pathway-2

The transition state search for pathway-2 was again carried out on a p(2x2), 6-layer Co vacuum slab model. *The initial reactant structure for this calculation consisted of a hydrogen atom in an octahedral void within the first sublayer and a methyl group adsorbed at a surface hcp site across a Co atom away from the hydrogen.* The final product structure is the same as shown in fig 4.6. The procedure for determing the transition

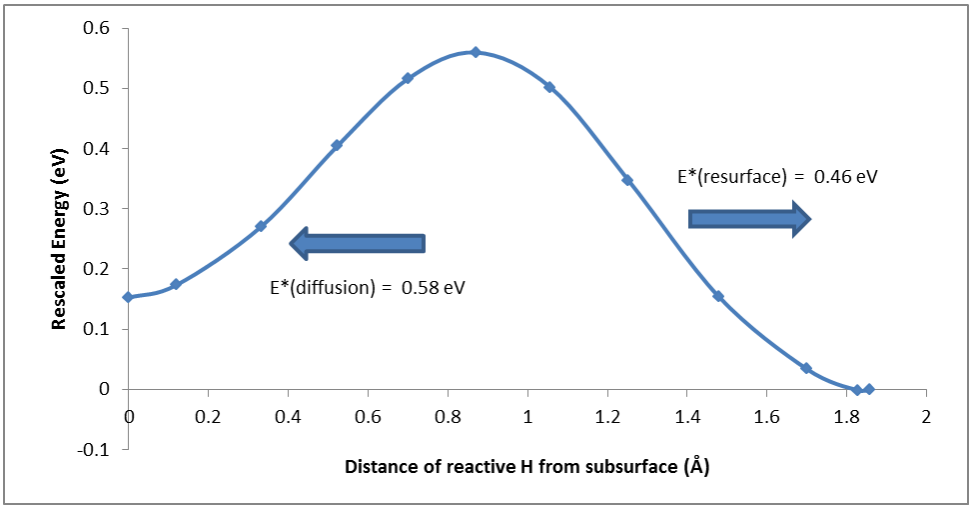

Figure 4.8: Minimum energy pathway depicting resurfacing of hydrogen from subsurface to surface (left to right on the X-axis) during methanation in pathway-1(methyl group adjacent to H resurfacing site) on Co(0001); Barriers E* include Zero Point Energy(see section 2.8.1) corrections. The reaction coordinate in this fig is defined as the distance of the reactive hydrogen from the subsurface site. A value of 0 Å would indicate that the hydrogen atom is between the surface layer and the first Co sublayer. The distance from the subsurface site is about 1.83 Å once the hydrogen reaches the surface.

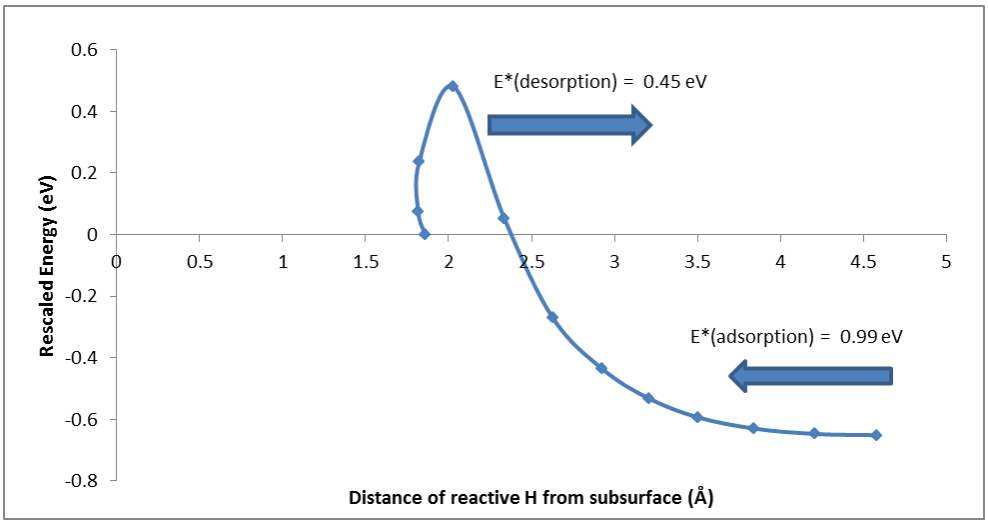

Figure 4.9: Minimum energy pathway depicting recombination of hydrogen with surface methyl group during methanation in pathway-1(methyl group adjacent to H resurfacing site); Barriers E* include Zero Point Energy(see section 2.8.1) corrections. The reactive hydrogen starts to move from the surface and combines with the adjacent methyl group to form methane which ultimately lies physisorbed at a distance of 4.5 Å.

states was similar to the one applied for pathway-1. After a coarse NEB run, once again two transition states (fig 4.11) were seen in the MEP. It was expected that they most likely would correspond again to a resurfacing and a recombination barrier. Hence, for this configuration of a reactant structure too, *no direct methanation pathway* was seen!

(a) Top view of Co(0001) surface with subsurface H atom and the methyl group adsorbed at a surface hcp site across a Co atom

(b) Side view of Co(0001) surface with subsurface H atom and the methyl group adsorbed at a surface hcp site across a Co atom

Figure 4.10: Initial reactant structure for pathway-2 on a p(2x2), 6-layered Co vacuum supercell, Blue-Co atoms, White-Hydrogen, Grey-Carbon

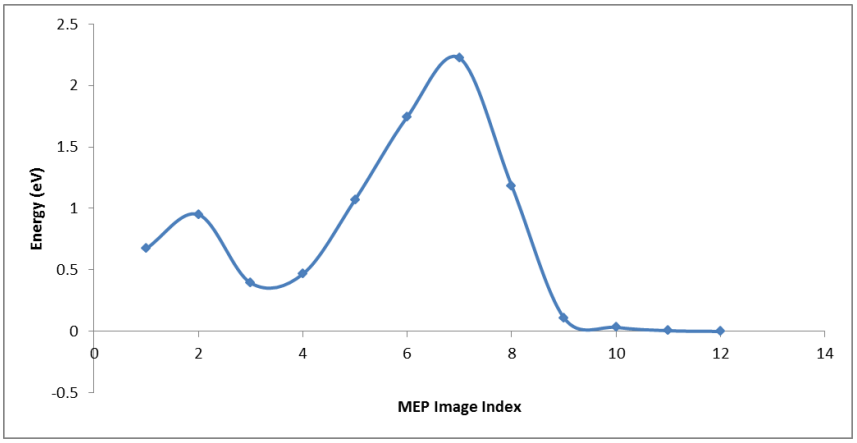

Figure 4.11: Rescaled energy vs image index for pathway-2; image index # 1 corresponds to the initial reactant structure as shown in fig 4.10 whereas the image index # 12 corresponds to the final product structure as shown in fig 4.6; Energies have been rescaled such that the product structure(with methane as in fig 4.6) is at 0 eV.

After splitting the pathway into two different NEB calculations, the activation barriers for the resurfacing and the recombination events were determined. The energies in the figures 4.12 and 4.13 have been rescaled to highlight the energy differences as we trace out the Minimum Energy Pathway (MEP).

The transition state for the resurfacing event was rigorously converged using the CI-NEB method at an accuracy of 0.02 eV/Å and that of the recombination was done at 0.04 eV/Å. The forward and the backward activation barriers with the adequate zero point energy (ZPE) corrections are listed in the figures itself. From the resurfacing site,

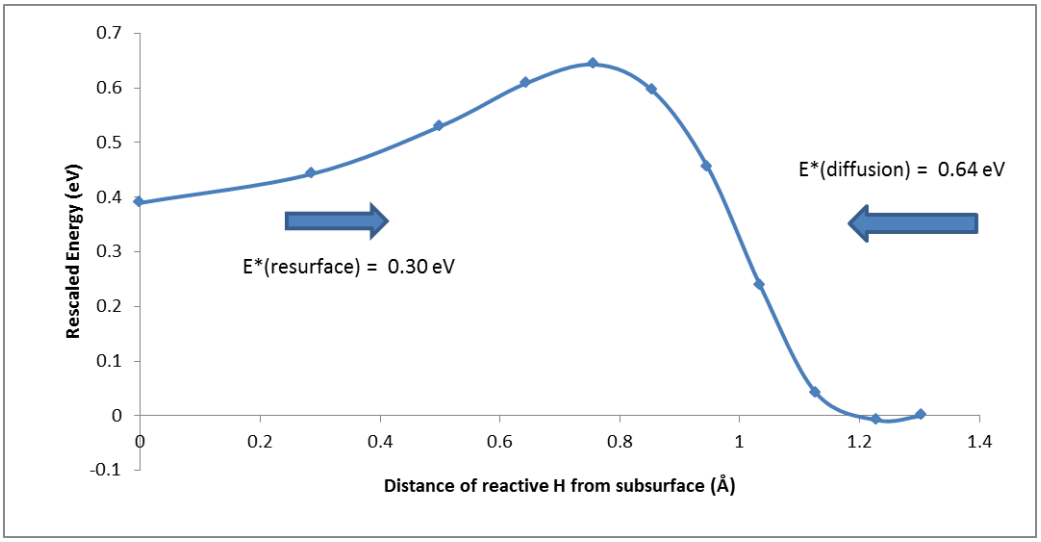

Figure 4.12: Minimum energy pathway depicting resurfacing of hydrogen from subsurface to surface (left to right on the X-axis) during methanation in pathway-2(methyl group across a Co atom from the H resurfacing site) on Co(0001); Barriers E* include Zero Point Energy(see section 2.8.1) corrections. The reaction coordinate in this fig is defined as the distance of the reactive hydrogen from the subsurface site. A value of 0 Å would indicate that the hydrogen atom is between the surface layer and the first Co sublayer as shown in fig 4.10-b. The distance from the subsurface site is about 1.3 Å once the hydrogen reaches the surface corresponding to the rightmost image point.

the hydrogen atom moves over an unstable bridge site before it recombines with the methyl group and hence we see another smaller barrier before the recombination TS in fig 4.13. The saddle points were verified by conducting a normal mode analysis and determining the imaginary frequency for the reactive hydrogen. Once again analysis of the transition state geometry (see appendix B.2) for the recombination event as shown in fig 4.13 revealed that the methyl group (valency = 1) has moved from the surface hcp site (Coordination number = 3) to the top of a nearby Co atom which is the atop site (coordination number = 1). This is in good agreement with the generalized framework developed for microscopic reaction pathways[6] which was discussed earlier.

4.2.5 Methanation pathway-3

The transition state search for pathway-3 was also carried out on a p(2x2), 6-layer Co vacuum slab model. The initial reactant structure (fig 4.14) for this calculation consisted of a hydrogen atom in an octahedral void within the first sublayer and a methyl group adsorbed at a surface fcc site directly above the hydrogen. Based on an intuitive guess, this configuration was expected by many[8] to yield the most dominant pathway for methane formation in case of Ni(111). We decided to test it for Co(0001) and make a better comparison with Ni(111).

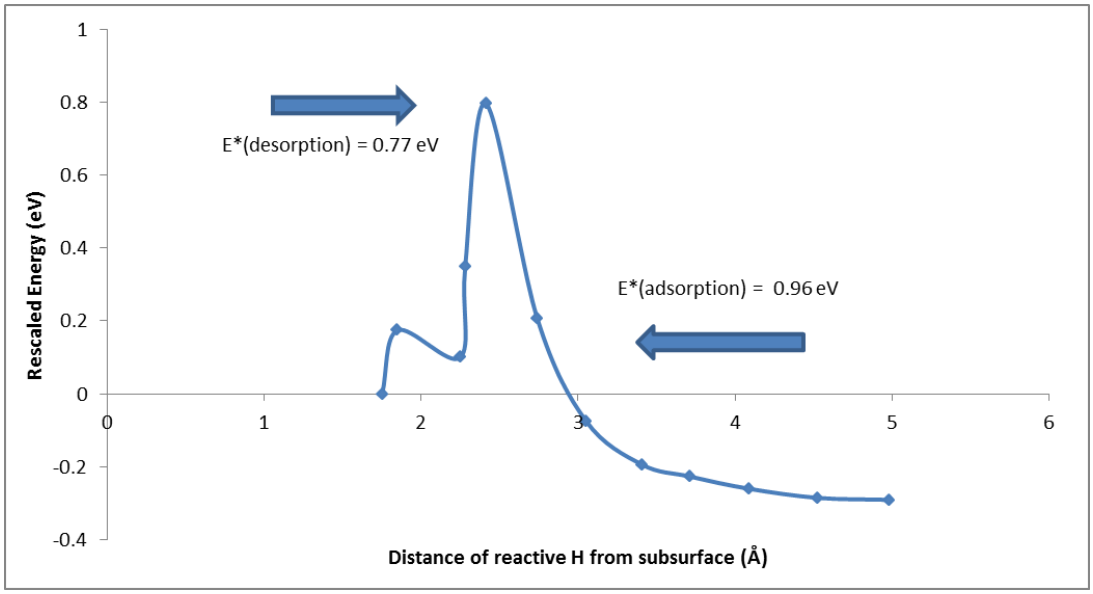

Figure 4.13: Minimum energy pathway depicting recombination of hydrogen with surface methyl group during methanation in pathway-2(methyl group across a Co atom from the H resurfacing site); Barriers E* include Zero Point Energy(see section 2.8.1) corrections. Each of the points(images) on the path(blue coloured) corresponds to a structure in which the reactive H is gradually approaching the methyl group with the rightmost final image corresponding to the product structure(fig 4.6) physisorbed at a distance of 5 Å.

(a) Top view of Co(0001) surface with adsorbed methyl group and subsurface H atom directly underneath

(b) Side view of Co(0001) surface with adsorbed methyl group and subsurface H atom directly underneath

Figure 4.14: Initial reactant structure for pathway-3 on a p(2x2), 6-layered Co vacuum supercell, Blue-Co atoms, White-Hydrogen, Grey-Carbon

The final product structure is again as shown in fig 4.6. The procedure for determing the transition states was similar to the one applied for pathway-1 and pathway-2. However, here only one TS (see appendix B.3) was seen.

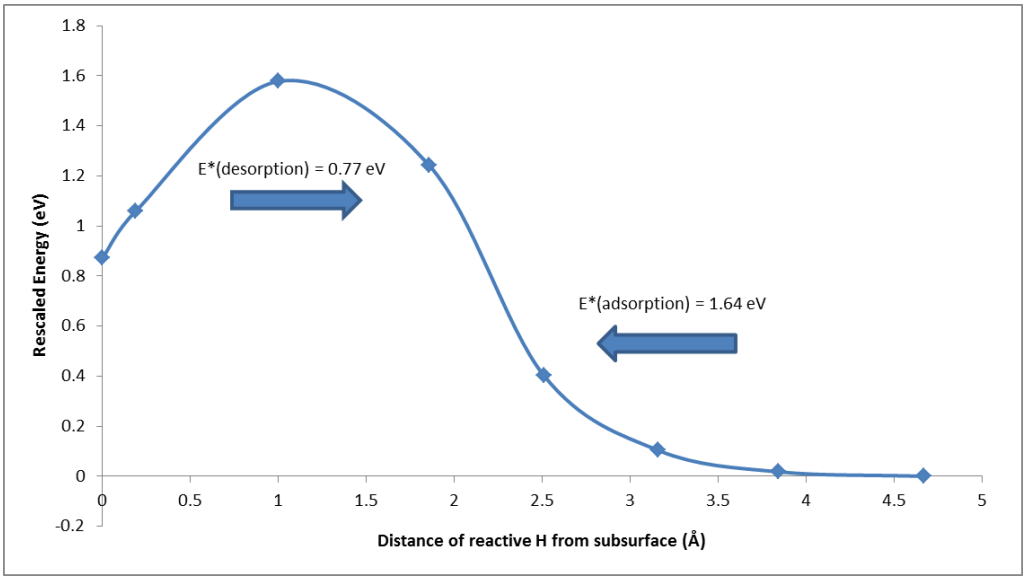

Figure 4.15: Minimum energy path depicting methanation in pathway-3(methyl group directly above the subsurface hydrogen) on Co(0001); Barriers E* include Zero Point Energy(see section 2.8.1) corrections. The reaction coordinate in this fig is defined as the distance of the reactive hydrogen from the subsurface site. A value of 0 Å would indicate that the hydrogen atom is between the surface layer and the first Co sublayer as shown in fig 4.14-b. Corresponding to the final image in which the hydrogen has combined with the methyl group to form the product structure with physisorbed methane(fig 4.6), the distance of the reactive hydrogen from the subsurface site is about 4.6 Å.

4.2.6 Comparison of methanation barriers between Co(0001) and Ni(111) catalysts

The activation barriers (without zero point energy corrections!) for methanation on Co(0001) are compared with those on Ni(111).[5] As we can see from table 4.5, the overall barrier for methanation is lowest for pathway-1 in case of Co(0001) which is also the case with Ni(111).[5] This pathway would statistically be the most dominant pathway for methanation on a Co(0001) surface. A more rigorous analysis regarding the prefactor estimation would give us a greater chemical insight.

	Pathway -1 (CH_3 adsorbed close to subsurface H site)		Pathway -2 (CH_3 adsorbed across the subsurface H site)		Pathway -3(CH_3 adsorbed on top of subsurface H site)
Catalyst surface	H resurfacing barrier (eV)	CH_4 desorption barrier(eV)	H resurfacing barrier (eV)	CH_4 desorption barrier (eV)	CH_4 desorption barrier (eV
Co(0001)	0.46	0.45	0.30	0.77	0.77
Ni (111)	0.56	0.09	0.49	0.79	1.36

Table 4.5: Ni(111)[5] vs Co(0001) methanation barriers for all the three pathways

4.3 Estimation of reaction rates based on hTST approximation

Using normal mode analysis and the hTST approximation,[7] the prefactors for methane formation via all the three pathways have been estimated as explained in section 2.9. The results (Table 4.6) indicate that methane formation would most likely occur through pathway-1.

Pathway -1 (CH_3 adsorbed close to subsurface H site)		Pathway -2 (CH_3 adsorbed across the subsurface H site)		Pathway -3(CH_3 adsorbed on top of subsurface H site)
H resurfacing prefactor ($10^{13} s^{-1}$)	CH_4 desorption prefactor ($10^{13} s^{-1}$)	H resurfacing prefactor ($10^{13} s^{-1}$)	CH_4 desorption prefactor ($10^{13} s^{-1}$)	CH_4 desorption prefactor ($10^{13} s^{-1}$)
1.57	5.14	1.04	1.82	1.19

Table 4.6: Prefactors for all three pathways at a temperature of 500 K

A better way to quantify this would be through the estimation of the rate constants which is shown in Table 4.7 after conducting a DFPT based vibrational analysis on the initial, final and the transition state structures.

Pathway -1 (CH_3 adsorbed close to subsurface H site)		Pathway -2 (CH_3 adsorbed across the subsurface H site)		Pathway -3(CH_3 adsorbed on top of subsurface H site)
H resurfacing rate constant (s^{-1})	CH_4 desorption rate constant (s^{-1})	H resurfacing rate constant (s^{-1})	CH_4 desorption rate constant (s^{-1})	CH_4 desorption rate constant (s^{-1})
1.6×10^8	6.7×10^8	5.8×10^9	7.9×10^4	5.2×10^4

Table 4.7: Rate constants for all three methanation pathways at T=500 K

The vibrational partition function was estimated as described in section 2.8.2 and the rate constant at a temperature of 500 K was calculated using equation (10) in section 2.8.1. As we can see in Table 4.7, the rate constants for pathway-1 are the highest compared to pathway-2 and pathway-3. For pathway-2, the recombination event(desorption) has a low rate constant which would be the rate-limiting step and hence would reduce the overall reaction probability. Thus, under the hTST approximation[7], we can infer that for a clean Co(0001) surface, pathway-1(CH_3adsorbed close to the subsurface hydrogen site) is the *most facile* pathway for methanation.

Chapter 5

Summary

5.1 Stability of subsurface hydrogen in the presence of CO

The presence of CO does not affect the adsorption energies of subsurface hydrogen. Hence, their stabilities[4] at the Fischer-Tropsch reaction conditions should *not* change much and they are very likely to participate in the methanation process.

5.2 Pathways for methane desorption

There exists no direct pathway for methanation involving subsurface hydrogen. For all the three pathways, the subsurface hydrogen first emerged on the surface site after crossing a resurfacing barrier and then combined with the surface methyl group to form methane. For pathway-3 where the adsorbed methyl directly encapped the subsurface hydrogen, as the hydrogen moves towards the surface, the methyl group also starts moving to an *on-top* position on a nearby Cobalt atom which is the transition state geometry for recombination. Hence, the MEP seems to contain only one overall transition state. However, a higher number of converged images in the NEB might reveal certain additional barriers. Pathway-1 in which the methyl group is adsorbed at a surface hcp site close to the subsurface hydrogen is statistically the most relevant. It has the lowest overall barrier and the based on a hTST based reaction rate approximation, the highest rate for methane desorption.

5.3 Path Forward

The next step would involve probing the behaviour of certain additives that would serve to increase the activation barriers for methanation. These additives would be site-specific such they tend to discourage the recombination of surface hydrogen and methyl group. Also, ab initio molecular dynamics studies can be used to clearly quantify the difference in activity for surface and subsurface hydrogen. The subsurface hydrogen emerges from a metastable state w.r.t the surface i.e it has higher energy. As it approches the surface, it loses this energy which might reappear in the from of it's kinetic energy and hence could make the recombination process more favourable. This might account for the high reactivity observed for subsurface hydrogen in Ni(111) as seen in Ceyer's[8] experiments.

References

[1] A Combined in-Situ PM-RAIRS and Kinetic Study of Single-Crystal Cobalt Catalysts under Synthesis Gas at Pressures up to 300 mbar; G. A. Beitel, C. P. M. de Groot, H. Oosterbeek, and J. H. Wilson. J.Phys.Chem. B 101 (1997)4035-4043

[2] J. J. C. Geerlings, J. H. Wilson, G. J. Kramer, H. P. C. E. Kuipers, A. Hoek, and H. M. Huisman. "Fischer–Tropsch technology—from active site to commercial process." Applied Catalysis A186, (1999)27-40.

[3] P. Giannozzi et al., J. Phys. Condens. Matter 21 395502 (2009); http://www.quantum-espresso.org

[4] Role of subsurface Hydrogen in methane selectivity in GTL and Insilico leads to suppress methane; A.Thyagarajan, S.van Bavel, H. kuipers, Shell Report 11.14275

[5] Physical origin of the high reactivity of subsurface hydrogen in catalytic hydrogenation; Michaelides, Hu and Alavi; J Chem Phys. 111, 1343 (1999)

[6] Insight into Microscopic Reaction Pathways in Heterogeneous Catalysis; A. Michaelides and P. Hu, J Am. Chem. Soc. 2000, 122, 9866-9867

[7] How to get Kinetic parameters, Lecture notes in Physics 856, An Introduction to KMC Simulations of Surface Reactions, Dr A.P.J. Jansen

[8] The Chemistry of Bulk Hydrogen: Reaction of Hydrogen embedded in Nickel with adsorbed CH_3; Johnson, Daley, Utz and Ceyer; SCIENCE, Vol 257, July 1992

[9] CH_x hydrogenation on Co(0001): A density functional theory study; The Journal Of Chemical Physics 122, 024711 (2005); doi: 10.1063/1.1829257

[10] Introduction to DFT- Juan Carlos Cuevas, Institut fur Theoretische Festkorperphysik Universitat Karlsruhe (Germany)

[11] Essentials of Computational Chemistry- Theories and Models, Christopher J Cramer

[12] David Vanderbilt- Rutgers University

[13] Theory of Condensed Matter, Cavendish Laboratory, University of Cambridge

[14] Special points for Brillouin-zone integrations; Monkhorst and Pack, Phys Rev B 13, 5188, June 1976

[15] A climbing image nudged elastic band method for finding saddle points and minimum energy paths; Henkelman, Uberuaga, Jonsson; Journal Of Chemical Physics, Vol 113, Number 22, Dec 2000

[16] Large-scale computing with Quantum ESPRESSO, P. Giannozzi (1),(2) and C. Cavazzoni (3); IL NUOVO CIMENTO Vol. 32 C, N. 2; (1) CNR-INFM DEMOCRITOS National Simulation Center - 34100 Trieste, Italy; (2) Dipartimento di Fisica, Universit'a di Udine - Via delle Scienze 208, I-33100 Udine, Italy; (3) CINECA - via Magnanelli 6/3, 40033 Casalecchio di Reno, Bologna, Italy

[17] Lecture slides on parallel computing, http://training.uhem.itu.edu.tr/docs/

[18] http://www.gipaw.net/

[19] Queen Mary, University of London.

[20] Kulik Tutorials on Quantum Espresso by Dr. Heather Kulik, MIT, USA

[21] Cobalt—Cobalt Multiple Bonds in Homoleptic Carbonyls? $Co_2(CO)_x$ (x = 5—8) Structures, Energetics, and Vibrational Spectra; Joseph P. Kenny, R. Bruce King, and Henry F. Schaefer; Inorg. Chem. 2001, 40, 900-911

[22] Infrared spectra of matrix-isolated dicobalt octacarbonyl, Evidence for the third isomer; Sweany, R. L.; Brown, T. L. Inorg. Chem. 1977, 16, 415

[23] Spinning-Cell FT-Raman Spectroscopy: Application to Crystalline Octacarbonyldicobalt(0), $Co_2(CO)_8$; Brienne,S.H.R.;Markwell, R. D.; Barnett, S. M.; Butler, I. S.; Finch,J. A. Appl. Spectrosc. 1993, 47, 1131.

[24] Ishii, M; Ahsbahs, H; Hellner, E; Schmid, G. Ber. Bunsen-Ges. Phys.Chem. 1979, 83, 1026

[25] First-principles extrapolation method for accurate CO adsorption energies on metal surfaces; Mason, Grinberg, Rappe, Phys. Rev. B 69 (2004)

[26] Gajdos, Eichler, Hafner, J. Phys Condens. Matter 16 (2004)

[27] Density-functional study of the CO adsorption on ferromagnetic Co(0001) and Co(111) surfaces; Stepan Pick, Surface Science 601 (2007); also see J.Lahtinen, J. Vaari, K. Kauraala, E.A Soares, M.A Van Hove, Surf Sci 448 (2000) 269

[28] Hydrogen Adsorption on Co surfaces: A Density Functional Theory and Temperature Programmed Desorption Study; Pieter van Helden, Berg, Weststrate; Sasol Technology Ltd, ACS Catal.. 2012, 2. 1097-1107

[29] J.Lahtinen, J. Vaari, K. Kauraala, E.A Soares, M.A Van Hove, Surf Sci 448 (2000) 269

Appendix A

Bloch theorem

We consider non-interacting particles in an effective Kohn-Sham potential $V_{KS}(r)$. In a perfect crystal, the nuclei are arranged in a regular periodic array described by a set of Bravais lattice vectors $\{R\}$. The potential is also periodic and can be described as

$$V(r+R) = V(r)$$

for all Bravais lattice vectors R. The Schrödinger equation which describes the motion of a single particle in this potential is $\left[\frac{-1}{2}\nabla^2 + V(r)\right]|\psi> = \varepsilon|\psi>$. The translation operators T_R are defined in such a way that they act on an arbitary function $f(r)$ in the following manner

$$T_R f(r) = f(r+R)$$

Because of the periodic potential used to describe the system, the Hamiltonian is also periodic. The translation and the Hamiltonian operators commute with each other i.e. $T_R H(r)\psi(r) = H(r)T_R\psi(r)$ which is also written as $[H(r), T_R] = 0$. It is thus possible to choose the eigenstates of the Hamiltonian to be the simultaneous eigenstates of all the translation operators which implies

$$H(r)\psi(r) = \varepsilon\psi(r)$$

$$T_R\psi(r) = C(r)\psi(r)$$

Since the translation operators commute with each other, we have the following relation for the eigen values $C(R+R^{'}) = C(R)C(R^{'})$. We can define the eigen values for the three primitive lattice vectors $\{a_i\}$ in terms of the three complex numbers $\{x_i\}$ by $c(a_i) = exp(2\pi i x_i)$. We know that any lattice vector can be written in the form $R = n_1a_1 + n_2a_2 + n_3a_3$ where the $n_i$are integers. This is equivalent to $c(R) = exp(ik \cdot R)$, $k = x_1g_1 + x_2g_2 + x_3g_3$where the $\{g_i\}$ are the reciprocal space lattice vectors which satisfy the relation $a_i \cdot g_j = 2\pi\delta_{ij}$ and the $\{x_i\}$ are complex numbers. Thus, the bloch theorem can also be stated as $T_R\psi(r) = \psi(r+R) = C(r)\psi(r) = exp(ik \cdot R)\psi(r)$. Now, we consider the function $U(r) = exp(-ik \cdot r)\psi(r)$. Translating this function we get $U(r+R) = exp(-ik \cdot (r+R))\psi(r+R) = exp(-ik \cdot r)\psi(r) = U(r)$. This suggests that $U(r)$ also has the periodicity of the lattice! Thus, the wavefunction can now be expressed as $\psi(r) = U(r)exp(ik \cdot r)$. The common eigen states of the Hamiltonian and the translation operators are named as $|\psi_{nk}>$ where n is a quantum number labelling different eigenstates

and k is a vector related to the translational symmetry. Since, a periodic function can always be expressed as a fourier series, we express $U(r)$ as

$$U(r) = \sum_G \acute{U}_G exp(iG \cdot r)$$

where G is the reciprocal space vector $G = m_1 g_1 + m_2 g_2 + m_3 g_3$ and the $m_i$are integers. The state $|\psi_{nk} >$ can now be expressed as a linear combination of plane waves :

$$\psi_{nk}(r) = exp(ik \cdot r) U_{nk}(r)$$

$$\psi_{nk}(r) = \sum_G C_{nk}(G) exp[i(k+G) \cdot r] \tag{A.1}$$

The main advantage here is that instead of solving for the wave function over all of infinite space, the problem now consists of solving the wave function within a single cell with infinitely many possible values of k. Upon application of necessary boundary conditions, the number of k-points are restricted to a *small region* and hence the computation process becomes much easier.

Appendix B

Transition state structures for methanation pathways on Co(0001)

B.1 Pathway-1

As shown in section 4.2.3, the initial reactant structure for this calculation consisted of a hydrogen atom in an octahedral void within the first sublayer and a methyl group adsorbed at a surface hcp site adjacent to the hydrogen. The existence of two saddle points for this entire pathway was confirmed from the MEP in fig 4.7. The entire path was split into two different MEPs corresponding to a resurfacing and a recombination barrier. The predicted transition state structures were subject to a DFPT based normal mode analysis, after which it was found that one of the vibrational modes of the subsurface hydrogen had an imaginary frequency. This further confirmed that we had indeed found a true transition state geometry.

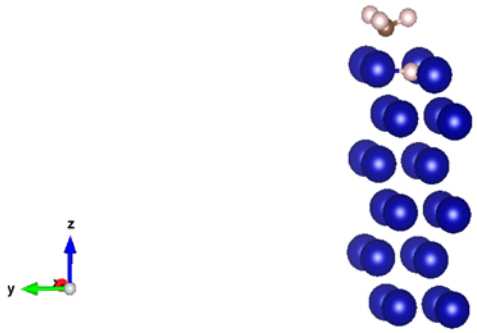

Figure B.1: TS structure for the subsurface hydrogen moving to the surface in pathway-1(side view).

B.2 Pathway-2

As shown in section 4.2.4, the initial reactant structure for this calculation consisted of a hydrogen atom in an octahedral void within the first sublayer and a methyl group adsorbed at a surface hcp site across a Co atom away from the hydrogen. The entire

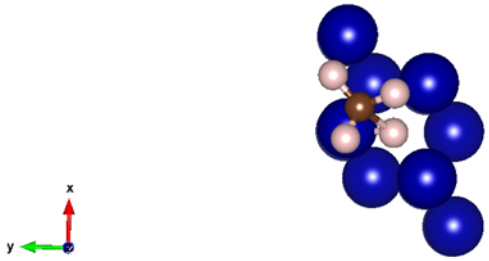

Figure B.2: TS structure (top view) for the recombination between surface hydrogen and surface methyl group in pathway-1; Note that the surface methyl group has almost moved to an on-top position (top of a Co atom on the surface).

path was split into two different MEPs corresponding to a resurfacing and a recombination barrier. Similar to pathway-1, the convergence to the transition states was verified after a rigorous DFPT based normal mode analysis.

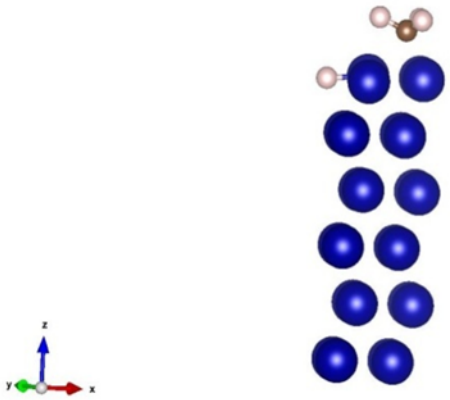

Figure B.3: TS structure for the subsurface hydrogen moving to the surface in pathway-2(side view).

B.3 Pathway-3

As described in section 4.2.5, the initial reactant structure (fig 4.14) for this calculation consisted of a hydrogen atom in an octahedral void within the first sublayer and a methyl group adsorbed at a surface fcc site directly above the hydrogen. Similar to pathway-1, the convergence to the single transition state was verified after a rigorous DFPT based normal mode analysis revealed the existence of an imginary frequency corresponding to the subsurface hydrogen.

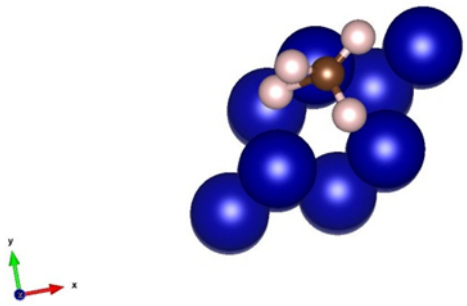

Figure B.4: TS structure for the recombination between surface hydrogen and surface methyl group in pathway-2 (top view); Note that the surface methyl group has moved to an on-top position which is consistent with the prediction mentioned earlier.[6]

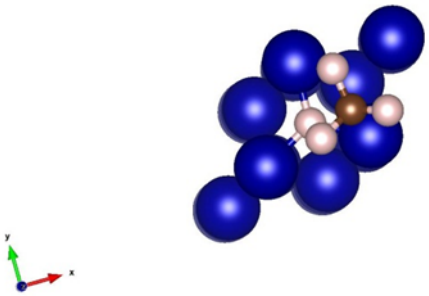

Figure B.5: TS structure for pathway-3 (top view) where the methyl group has moved to a nearby on-top site and made way for the subsurface hydrogen to emerge on the surface fcc site.